Stiffness threshold of randomly distributed carbon nanotube networks

Yuli Chen [a,b,*], Fei Pan [a], Zaoyang Guo [a,b], Bin Liu [c], Jianyu Zhang [d]

[a] Institute of Solid Mechanics, Beihang University (BUAA), Beijing 100191, PR China
[b] International Research Institute for Multidisciplinary Science, Beihang University (BUAA), Beijing 100191, PR China
[c] AML, CNMM, Department of Engineering Mechanics, Tsinghua University, Beijing 100084, PR China
[d] College of Aerospace Engineering, Chongqing University, Chongqing 400044, PR China

ARTICLE INFO

ABSTRACT

For carbon nanotube (CNT) networks, with increasing network density, there may be sudden changes in the properties, such as the sudden change in electrical conductivity at the electrical percolation threshold. In this paper, the change in stiffness of the CNT networks is studied and especially the existence of stiffness threshold is revealed. Two critical network densities are found to divide the stiffness behavior into three stages: zero stiffness, bending dominated and stretching dominated stages. The first critical network density is a criterion to judge whether or not the network is capable of carrying load, defined as the stiffness threshold. The second critical network density is a criterion to measure whether or not most of the CNTs in network are utilized effectively to carry load, defined as bending–stretching transitional threshold. Based on the geometric probability analysis, a theoretical methodology is set up to predict the two thresholds and explain their underlying mechanisms. The stiffness threshold is revealed to be determined by the statical determinacy of CNTs in the network, and can be estimated quantitatively by the stabilization fraction of network, a newly proposed parameter in this paper. The other threshold, bending–stretching transitional threshold, which signs the conversion of dominant deformation mode, is verified to be well evaluated by the proposed defect fraction of network. According to the theoretical analysis as well as the numerical simulation, the average intersection number on each CNT is revealed as the only dominant factor for the electrical percolation and the stiffness thresholds, it is approximately 3.7 for electrical percolation threshold, and 5.2 for the stiffness threshold of 2D networks. For 3D networks, they are 1.4 and 4.4. And it also affects the bending–stretching transitional threshold, together with the CNT aspect ratio. The average intersection number divided by the fourth root of CNT aspect ratio is found to be an invariant at the bending–stretching transitional threshold, which is 6.7 and 6.3 for 2D and 3D networks, respectively. Based on this study, a simple piecewise expression is summarized to describe the relative stiffness of CNT networks, in which the relative stiffness of networks depends on the relative network density as well as the CNT aspect ratio. This formula provides a solid theoretical foundation for the design optimization and property prediction of CNT networks.

© 2015 Elsevier Ltd. All rights reserved.

* Corresponding author at: Institute of Solid Mechanics, Beihang University (BUAA), Beijing 100191, PR China.
  E-mail address: yulichen@buaa.edu.cn (Y. Chen).

1. Introduction

Researchers have been seeking a way to transfer the excellent properties of Carbon Nanotubes (CNTs) in nanoscale to macro-materials (Bryning et al., 2007; Kim et al., 2011; Lu et al., 2012; Wang et al., 2012; Xie et al., 2011; Xu et al., 2010). It has been found that isolated CNTs can hardly make great improvements in mechanical properties of macroscale materials (Ma et al., 2009; Moniruzzaman and Winey, 2006). Recent studies show that CNT constructed networks, such as films (Wu et al., 2004; Zhang et al., 2005), sponges (Gui et al., 2010) and foams (Cao et al., 2005), are probably an effective material structure form to utilize CNTs in macroscale applications, hence drawing many attentions.

CNT constructed networks process many unique properties (e.g. low density and high porosity) and therefore have wide potential applications, such as CNT conductive coatings for lightning protection and electromagnetic interference shielding (Gagné and Therriault, 2014; Gou et al., 2010; Yang et al., 2005), CNT membrane filters for water and air purification (Brady-Estévez et al., 2008; Cooper et al., 2003; Halonen et al., 2010; Li et al., 2013; Smajda et al., 2007; Viswanathan et al., 2004), catalyst supports (Halonen et al., 2010; Zhu et al., 2010), artificial muscles (Aliev et al., 2009; Foroughi et al., 2011; Vohrer et al., 2004) and gas sensor (Sayago et al., 2008; Slobodian et al., 2011).

Experimental studies have exhibited that the formation of CNT networks may lead to sudden changes in properties of their macro-materials. For example, the electrical percolation threshold of CNT/polymer composites is observed experimentally (Allaoui et al., 2002; Gojny et al., 2006; Koerner et al., 2005; Kovacs et al., 2007; Moisala et al., 2006). The composites are conductive only when the volume fraction of CNTs in the composites is higher than the threshold. And furthermore, once the CNT volume fraction reaches the threshold, the conductivity of the composites increases rapidly. This sudden change as well as the electrical percolation threshold is predicted by studying the topology of the network (Chen et al., 2015a; Lu et al., 2010). The question then arises: does this threshold behavior also exist in mechanical properties of CNT networks? As for mechanical properties, a similar stepwise sudden change is found in the fracture toughness study on CNT reinforced composites: the main failure mode is converted from CNT pull-out to CNT break with an increase in interface strength, and the fracture toughness also declines suddenly during this transition (Chen et al., 2010, 2015b). This phenomenon is also identified experimentally by other researchers (Tang et al., 2011a, 2011b). Besides, a sudden increase in stiffness of compressed exfoliated graphite as well as nanocomposites is captured in experiments and simulations (Baxter and Robinson, 2011; Celzard et al., 2005). The critical value for this sudden increase is considered to be consistent with the electrical percolation threshold, although the sudden increase in stiffness can hardly explained by the mechanism of electrical percolation threshold.

Therefore, it is reasonable to guess that increasing CNT volume fraction in CNT networks may lead to sudden change in their mechanical properties. The aims of this paper are to reveal the stiffness threshold mechanism for randomly distributed CNT networks, and to establish the relation between topology and stiffness of CNT networks, which may be readily used to guide the design optimization and strength analysis in practical applications. This paper is structured as follows. First, the topology analysis on load-transfer paths and defect fraction of 2-dimensional (2D) CNT networks is carried out to reveal the mechanism of load-carrying capacity of CNT networks and the existence of stiffness threshold and bending–stretching transitional threshold in Sections 2 and 3, respectively. The invariants at the two thresholds are derived based on the geometric probability analysis on the average intersection number of each CNT in the network, and validated by the numerical simulations. Subsequently, in Section 4, the expression to describe the three-stage behavior of CNT network stiffness is established based on the two thresholds. The methodology to estimate the stiffness and thresholds of CNT networks are extended to 3-dimensional (3D) CNT networks in Section 4.4 and a brief summary is given in Section 5.

2. Stiffness threshold versus electrical percolation threshold

Based on the previous studies and the subsequent simulations, considering both the electrical and mechanical properties, the CNT networks may present 4 different types of behaviors with increasing network density, as illustrated in Fig. 1: (1) neither electrical conductive nor able to carry load; (2) electrical conductive but not able to carry load; (3) electrical conductive and able to carry load by bending dominated deformation; and (4) electrical conductive and able to carry load by stretching dominated deformation. The critical value between type 1 and type 2 is the electrical percolation threshold, and the critical value between type 2 and type 3 is defined as the stiffness threshold in this paper. In this section, we will focus on these two values, and the last critical value will be studied in Section 3.

2.1. Qualitative analysis on stiffness threshold

The electrical percolation threshold has been intensively studied by both theoretical and experimental approaches (Balberg et al., 1984; Bauhofer and Kovacs, 2009), and most researchers have reached a consensus that the composite is conductive only when the conductive path is formed. The lowest CNT volume fraction to form the conductive path is defined as the electrical percolation threshold.

Similarly, the load-transfer path must be constructed so that the CNT networks can carry load; otherwise, without load-transfer path, the network cannot carry load, and the stiffness of the network is zero. Therefore, for the CNT networks with low density, there should be a critical CNT volume fraction at which the stiffness becomes nonvanishing. This critical CNT
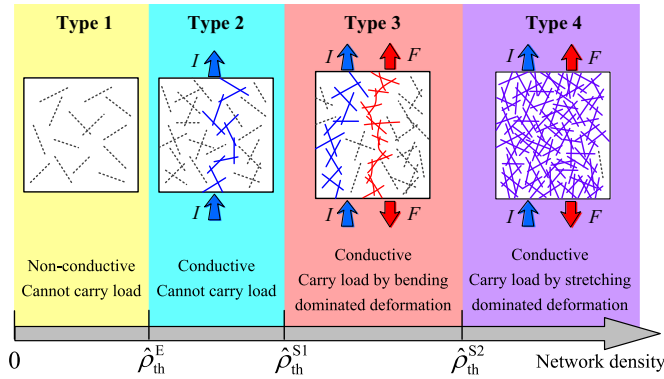
Fig. 1. Overall view on the four types of electrical and mechanical properties of CNT networks, with three critical values: electrical percolation threshold $\hat{\rho}_{th}^{E}$, stiffness threshold $\hat{\rho}_{th}^{S1}$, and the bending–stretching transitional threshold $\hat{\rho}_{th}^{S2}$.

volume fraction is defined as stiffness threshold.

Some researchers think that the CNT networks can carry load if the electrical percolation threshold is reached (Berhan et al., 2004b). However, for most CNT constructed networks without matrix material, the interactions between two CNTs are not strong enough to suppress the relative rotation between tubes due to the tiny interacting area, even if the CNTs are connected by chemical bonds and junctions (Stormer et al., 2012). Therefore, when the conductive path is formed, the CNTs that compose the path are still loose and cannot carry load. Only when the interactions between CNTs are strong enough to form a rigid connection, the stiffness threshold can be estimated as the electrical percolation threshold. Hence the electrical percolation threshold is the lower limit of stiffness threshold. A new model is required to predict the stiffness threshold accurately for CNT networks.

Furthermore, the increasing behavior of the stiffness of CNT networks after the stiffness threshold is very different from that of the electrical conductivity after the electrical percolation threshold. For the network electrical conductivity, every single CNT in the network is either conductive or non-conductive, so the contribution of single CNT increases like a step, and the conductivity of the whole network increases with only the increasing number of conductive CNTs. However, for the network stiffness, the load-carrying capacity of each CNT in networks increases gradually and continuously, until reaches its saturation point, which is the axial stretching stiffness of CNT. Therefore, after the stiffness threshold, firstly, the stiffness of the whole network depends on both the number of CNTs that can carry load and the load-carrying capacity of each CNT, and then, when all the CNTs reach their saturation points, the network stiffness depends only on the number of CNTs. Accordingly, at the stiffness threshold, the network stiffness increases with an exponent higher than that for the network conductivity at the percolation threshold. In addition, the exponent for increasing network stiffness becomes lower at the saturation point, while the exponent for network conductivity is a constant. This difference in exponent will be discussed in detail in Section 4.

2.2. Theoretical model for stiffness threshold

In many applications, such as CNT conductive coatings and CNT membrane filters, the size of CNT networks of one dimension is significantly smaller than those of the other two dimensions, and the networks thus can be considered as 2D networks. Here we will first focus on the stiffness of 2D CNT networks, and then extend the methodology to 3D CNT networks in Section 4.4.

2.2.1. Definition of stabilization fraction

Previous studies have shown that the interactions between pristine CNTs, such as van der Waals interactions and electrostatic interactions, are too weak to transfer load efficiently (Chen et al., 2011; Xie et al., 2011). Therefore, the normally-used CNT networks are constructed by CNTs with inter-tube connections, such as nano-welding junctions (Banhart, 2001; O'Brien et al., 2013a, 2013b; Piper et al., 2011; Stormer et al., 2012) and chemical bonds (Chiu et al., 2002; Zhang et al., 2014), which can greatly improve the mechanical properties of networks. Hence our study focuses on the CNT networks with inter-tube connections.

Researchers have found that neither nano-welding junction nor chemical bond can provide a steady constraint to restrain the relative rotation between two CNTs, although they can restrain the relative sliding effectively (Stormer et al., 2012). Therefore, an inter-tube connection is considered as a "hinge" between two CNTs in this study. Three CNTs interacting with one another construct a triangle with three hinges, and the triangle is a geometrically stable configuration for load carrying (Ellenbroek and Mao, 2011; Jacobs and Thorpe, 1996). Consequently, the three CNTs are considered stable. Besides, if a CNT interacts with two of the forming-triangle CNTs, another triangle is formed and thus the CNT is also stable. The stable and unstable CNTs are demonstrated in Fig. 2 by solid and dashed line segments respectively. Each CNT triangle can be considered as the nucleus of a stable CNT clusters, and all stable CNTs may construct one or several stable clusters.
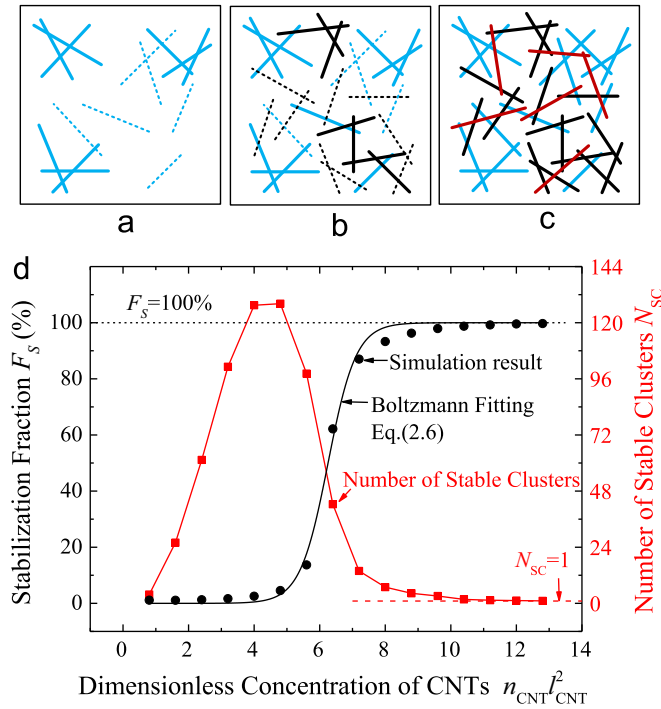
Fig. 2. Stabilization fraction of 2D CNT networks (solid and dashed line segments in (a)–(c) represent stable and unstable CNTs respectively): (a) nucleation of stable clusters, (b) small stable clusters coalescing to larger one with adding new CNTs (black ones), (c) the whole network becoming stable by adding only several CNTs (red ones), and (d) the stabilization fraction and number of stable clusters versus CNT concentration. (For interpretation of the references to color in this figure legend, the reader is referred to the web version of this article.)

According to the geometric invariance principle of structural analysis (Timoshenko and Young, 1945), under arbitrary loadings, only the structure with invariant geometry can carry and transfer loads. It is reasonable to assume that only stable CNTs contributes to the load-carrying capacity of the network. Generally, the largest stable CNT cluster dominates the load-carrying ability of the whole network. Denoting the number of CNTs that compose the largest stable cluster by N_{LSC}, the stabilization fraction F_S is then defined as

$$F_S = N_{LSC}/N_{CNT}. \tag{2.1}$$

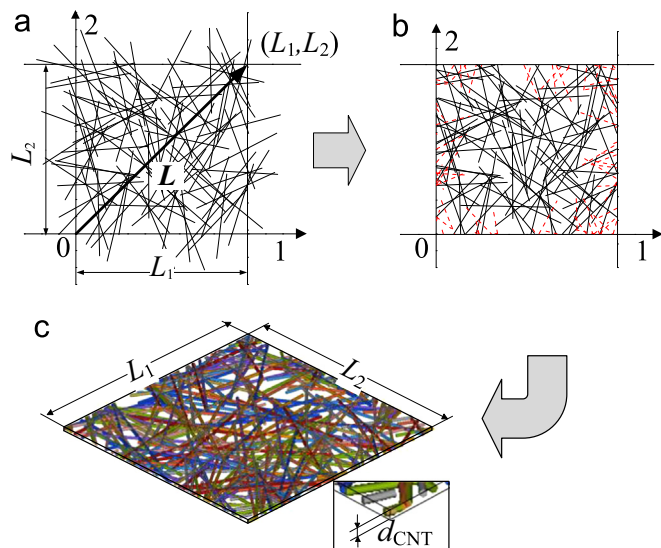where N_{CNT} is the total number of the CNTs in the network.

Fig. 3. 2D randomly distributed CNT network: (a) schematic diagram of a 2D CNT network before periodicity process, (b) schematic diagram of the 2D CNT network after periodicity process, and (c) FEM simulation model.

2.2.2. Studies on stabilization fraction

Microscopy images of CNT membranes show that the CNTs are distributed randomly in the membrane plane (Li et al., 2013; Wu et al., 2004), and the 2D simulation model is accordingly established, as shown in Fig. 3.

In the representative area element of CNT network in Fig. 3(a), CNTs are simplified as line segments with the length l_{CNT}, and the position and orientation of the CNTs are determined by the midpoint (X_1, X_2) and the angle θ. In a given area $L_1 \times L_2$, X_1, X_2 and θ follow uniform distributions in the ranges of $[0, L_1)$, $[0, L_2)$ and $[0, \pi)$, respectively. Assuming the unit cell is a periodic section in the whole network, the parts of CNTs outside the area $L_1 \times L_2$ should be moved inside the area following the equations below:

$$x_\alpha = \begin{cases} x_\alpha^{old} - L_\alpha, & x_\alpha^{old} > L_\alpha \\ x_\alpha^{old} + L_\alpha, & x_\alpha^{old} < 0 \qquad (\alpha = 1, 2), \\ x_\alpha^{old}, & 0 < x_\alpha^{old} < L_\alpha \end{cases}$$

(2.2)

where x^{old} and $\boldsymbol{x}$ are the coordinates of the points composing the line segments before and after the periodicity process, respectively, and $\boldsymbol{L}$ is the diagonal vector of the area $L_1 \times L_2$. Fig. 3(b) shows the periodic unit cell, in which the red dashed line segments are those moved from outside to inside.

The density for a 2D CNT network is defined as

$$\rho_N = \frac{\rho_{CNT} N_{CNT} l_{CNT} d_{CNT}}{L_E^2},$$

(2.3)

where ρ_{CNT} is the density of CNTs, N_{CNT} is the total number of the CNTs in the periodic unit cell, d_{CNT} is the diameter of CNTs, and $L_1 = L_2 = L_E$ is taken for simplicity. It should be noted that the moved CNTs (red dashed line segments in Fig. 3(b)) do not count as new ones.

The relative network density, or the CNT area fraction in the unit cell, is then defined as

$$\hat{\rho} = \frac{\rho_N}{\rho_{CNT}} = \frac{N_{CNT} l_{CNT} d_{CNT}}{L_E^2} = \frac{n_{CNT} l_{CNT}^2}{\lambda_{CNT}},$$

(2.4)

where $\lambda_{CNT} = l_{CNT}/d_{CNT}$ is the aspect ratio of CNTs, and $n_{CNT} = N_{CNT}/L_E^2$ is the number of CNTs in a unit area.

For 2D networks, if the aspect ratio λ_{CNT} is large enough, the diameter effect on the topology of network can be ignored. Thus the combined dimensionless parameter $(n_{CNT} l_{CNT}^2)$, which is the average CNT number in the area of $l_{CNT} \times l_{CNT}$, is defined as the CNT concentration to study the topology. According to the scaling law, the intersection relation of CNTs in the network depends only on the number of CNTs in the area of $l_{CNT} \times l_{CNT}$ (Kellomäki et al., 1996), which is exactly the CNT concentration $(n_{CNT} l_{CNT}^2)$.

The Monte Carlo simulation results of the stabilization fraction F_S versus the CNT concentration $(n_{CNT} l_{CNT}^2)$ are shown in Fig. 2(d) (with simulation details in Appendix A). It is found that the stabilization fraction F_S increases with the increase of CNT concentration $(n_{CNT} l_{CNT}^2)$, presenting an "S" shape. The S-shape curve indicates three stages of the behavior of the stabilization fraction F_S, which are nucleating, coalescing and stabilizing, similar to the process of water freezing to ice (Matsumoto et al., 2002). For the example shown in Fig. 2(d), when $(n_{CNT} l_{CNT}^2)$ is between 0 and 5, stabilization fraction F_S maintains in a very low level. In this stage, the triangle nucleuses of stable clusters begin to form, the number of stable nucleuses increases rapidly, but the largest stable cluster grows slowly, as illustrated in Fig. 2(a). At about $(n_{CNT} l_{CNT}^2) = 5$, the number of stable clusters reaches its maximum value. Then, as illustrated in Fig. 2(b), when adding CNTs into the network, the small stable clusters begin to coalesce into larger ones, so the number of stable clusters reduces and the size of the largest stable cluster grows rapidly, leading to a sharp increase in stabilization fraction F_S. When $(n_{CNT} l_{CNT}^2)$ becomes larger than 8, a dominated stable cluster forms, and the number of stable clusters decreases to about 1, while the stabilization fraction F_S increases slowly and converges to 100% gradually.

This S-shape curve can be described by Boltzmann function, written as

$$F_S = F_{S2} - \frac{F_{S2} - F_{S1}}{1 + \exp\left[\frac{4K(n_{CNT} l_{CNT}^2 - C_0)}{F_{S2} - F_{S1}}\right]}$$

(2.5)

Here F_{S1} and F_{S2} are the minimum and maximum values of F_S and should be set as 0 and 1, respectively, C_0 is the horizontal coordinate of the center of the central symmetrical Boltzmann curve and satisfies the relation $F_S|_{n_{CNT} l_{CNT}^2 = C_0} = (F_{S1} + F_{S2})/2$, and K is the slope at the center point.

If the unit cell size is not large enough relative to the CNT length, the S-shape curve is influenced by the relative size $\hat{L} = L_E/l_{CNT}$. The size effect and convergence study are carried out in Appendix B, and it is found that the curve converges when $\hat{L} \geq 20$. The converged Boltzmann fitting of stabilization fraction F_S is

$$F_S = 1 - \frac{1}{1 + \exp\left[2.342(n_{CNT} l_{CNT}^2 - 6.255)\right]}.$$

(2.6)

Substituting Eq. (2.4) into Eq. (2.6), we obtain

$$F_S = 1 - \frac{1}{1 + \exp\left[2.342\left(\hat{\rho}\lambda_{CNT} - 6.255\right) \right]}.$$

(2.7)

2.2.3. Predicting stiffness threshold by stabilization fraction

The stiffness threshold is defined as the lowest relative network density for the network capable of carrying load, denoted by $\hat{\rho}_{th}^{S1}$. In other words, at $\hat{\rho}_{th}^{S1}$, almost all CNTs in the network are just connected together to form a stable structure. It is thus reasonable to believe that the stabilization fraction is very close to 100% at $\hat{\rho}_{th}^{S1}$, which means $\hat{\rho}_{th}^{S1}$ corresponds to the start of the third stage of the S-shape curve in Fig. 2(d). The conversion from coalescing stage to stabilizing stage reflects the change in topological structure of the network, which leads to the transition in stiffness behavior at $\hat{\rho}_{th}^{S1}$.

Here the critical stabilization fraction $F_S^C = 99\%$ is taken as the criterion to predict the stiffness threshold $\hat{\rho}_{th}^{S1}$ of CNT networks as

$$\hat{\rho}_{th}^{S1} = \frac{\left(n_{CNT} l_{CNT}^2 \right)\big|_{F_S=99\%}}{\lambda_{CNT}} = \frac{8.2}{\lambda_{CNT}}.$$

(2.8)

The electrical percolation threshold can be obtained using the excluded volume method (Balberg et al., 1984) as

$$\hat{\rho}_{th}^{E} = \frac{5.8}{\lambda_{CNT}}.$$

(2.9)

Therefore the electrical percolation threshold $\hat{\rho}_{th}^{E}$ is about 29% lower than the stiffness threshold $\hat{\rho}_{th}^{S1}$. The main significance of the stiffness threshold $\hat{\rho}_{th}^{S1}$ is that the stiffness of network structures is required to maintain the normal functions of CNT networks since the mechanical failure may lead to the failure of other material functions. Hence, in many engineering applications, the stiffness threshold $\hat{\rho}_{th}^{S1}$ rather than the electrical threshold $\hat{\rho}_{th}^{E}$ provides the lowest network density to reach the mechanical requirement, especially for low-density multi-functional networks.

In addition, using Eq. (2.4), the average intersection number of each CNT in the network, which is obtained in Appendix C, is expressed as

$$\bar{N}_{int} = \frac{2}{\pi}\left(n_{CNT} l_{CNT}^2 \right) = \frac{2}{\pi}\hat{\rho}\lambda_{CNT}.$$

(2.10)

Thus the stiffness threshold $\hat{\rho}_{th}^{S1}$ can also be estimated by the average intersection number of each CNT in the network as

$$\bar{N}_{int}\big|_{\hat{\rho}_{th}^{S1}} = \frac{2}{\pi}\hat{\rho}_{th}^{S1}\lambda_{CNT} = 5.2,$$

(2.11)

while the average intersection number $\bar{N}_{int}$ is only 3.7 at the electrical percolation threshold $\hat{\rho}_{th}^{E}$ (Balberg et al., 1984).

As shown in Eqs. (2.8) and (2.11), the stiffness threshold is inversely proportional to the aspect ratio of CNTs, while the average intersection number at the threshold does not change. Therefore, the average intersection numbers per CNT at the stiffness thresholds can be considered as a useful invariant to predict the stiffness threshold. Similarly, according to Eq. (2.9), the electrical percolation threshold can also be estimated by an invariant average intersection number 3.7.

Therefore, no matter in mechanisms or values, the stiffness threshold is very different from the electrical percolation threshold. At the electrical percolation threshold, the possibility to form load-transfer path is very low. Hence it is unsafe in the network designs and practical applications to use the electrical percolation threshold $\hat{\rho}_{th}^{E}$ instead of the stiffness threshold $\hat{\rho}_{th}^{S1}$ to evaluate the mechanical properties of networks, especially for low-density multi-functional networks.

2.3. Numerical validation

At the stiffness threshold $\hat{\rho}_{th}^{S1}$, the modulus of network should possess the following two features simultaneously: (1) the network modulus is very close to zero and (2) the network can carry load, which means almost all different random distributions of the CNT networks can carry load. The finite element method (FEM) is employed here to simulate the tensile stiffness of CNT networks, with details in Appendix D. The network tensile modulus E_N can be obtained from the stress–strain relations of the CNT networks under uniaxial tension in the FEM simulations. Due to the random distribution of CNTs, from the view of statistics, the networks can be considered as isotropic materials. Without loss of any generality, the network is stretched in direction 1 with a given strain ε_{11}, and the total force along direction 1 can be obtained from the simulation, denoted as F_1. The network tensile stiffness E_N is then expressed as

$$E_N = \frac{F_1}{\varepsilon_{11} t L_2},$$

(2.12)

where $t = d_{CNT}$ is the thickness of the network.

For comparison, the normalized tensile modulus $\hat{E}$ is defined as the ratio of the network tensile modulus E_N to the CNT
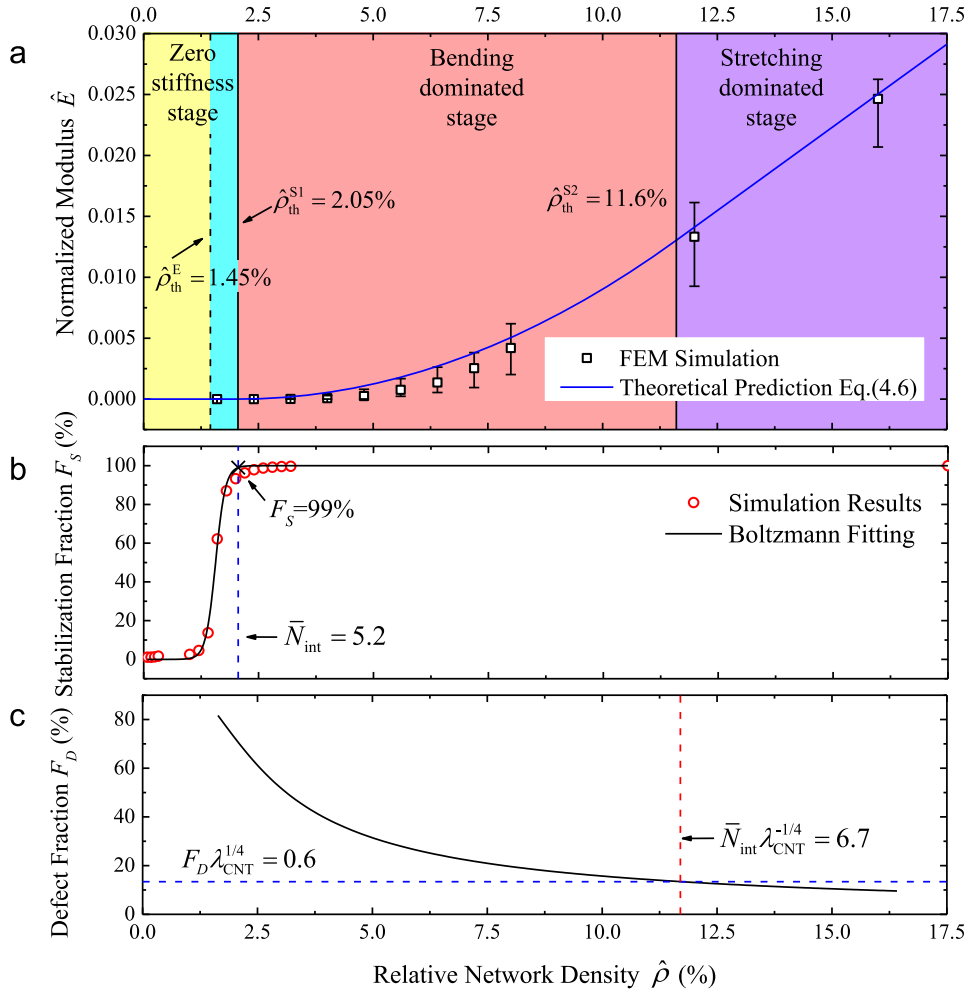
Fig. 4. Curves of (a) normalized tensile modulus, (b) stabilization fraction and (c) defect fraction versus the relative density of 2D networks with CNT aspect ratio $\lambda_{CNT} = 400$.

axial modulus E_{CNT}

$$\hat{E} = \frac{E_N}{E_{CNT}}. \tag{2.13}$$

Fig. 4(a) presents the FEM results of the mean value of normalized tensile modulus $\hat{E}$ versus the relative network density $\hat{\rho}$. The length and diameter of CNTs are 4 μm and 0.01 μm, respectively. More than 30 different networks with randomly distributed CNTs are generated by a pre-process code for each given network density and then simulated for the normalized tensile moduli of the networks. Comparing the FEM results in Fig. 4(a) and the theoretical prediction in Fig. 4(b), it can be found that the normalized tensile modulus $\hat{E}$ is almost zero when the stabilization fraction $F_S^C = 99\%$. Besides, the average normalized modulus at $F_S^C = 99\%$ for networks with different l_{CNT} and d_{CNT} are listed in Table 1. In Table 1, the average

Table 1

Simulation results on normalized tensile modulus $\hat{E}$ of 2D networks at the stiffness threshold with different CNT lengths and diameters.

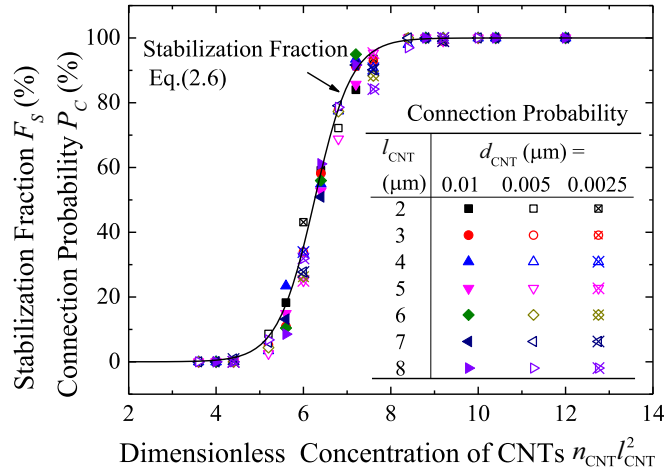| l_{CNT} (μm)	$d_{CNT}=0.01$ μm	$d_{CNT}=0.005$ μm	$d_{CNT}=0.0025$ μm
2	1.24E−6	1.29E−7	1.89E−8
3	3.53E−7	3.68E−8	5.81E−9
4	1.50E−7	1.41E−8	2.64E−9
5	7.30E−8	7.71E−9	1.23E−9
6	4.64E−8	4.33E−9	6.86E−10
7	2.75E−8	3.17E−9	4.79E−10
8	1.89E−8	1.85E−9	2.86E−10

Fig. 5. The connection probability of load-carrying paths of CNT networks with different length and diameter (markers), which is in good agreement with the stabilization fraction (curve).

normalized network modulus at $F_S^C = 99\%$ is very close to zero (three or more orders lower than the whole-range modulus of networks), although it increases with the decrease of CNT aspect ratio. Therefore, the criterion of stabilization fraction $F_S^C = 99\%$ satisfies the first feature of stiffness threshold.

For N_{test} times of FEM simulations with different random distribution, N_{test} output moduli are obtained from the computed tensile loads. When the network density is around the stiffness threshold, these output moduli can be divided into two groups according to their magnitudes, and all the moduli in one group are over 3 orders of magnitude larger than those in the other. Therefore, for the network in the former group, the load-transfer path is constructed and the network can carry load. On the other hand, for networks in the latter group, the extremely tiny values are just the numerical outputs due to the indeterminacy of the network structures. There is actually no load-transfer path in the network and the modulus of the network in the latter group is considered as zero when calculating the average modulus. Supposing the number of moduli in the larger-magnitude group is N_c, the connection probability of load-transfer path can be defined as

$$P_C = \frac{N_c}{N_{test}}.$$

(2.14)

When the connection probability P_C is close to 100%, almost all different random distributions of the CNTs can carry load, which exactly satisfies the second feature of stiffness threshold.

The connection probability results from the FEM simulations are illustrated in Fig. 5 for different networks with CNT diameter $d_{CNT} = 0.01$, 0.005 and 0.0025 μm and CNT length $l_{CNT} = 2–8$ μm. The simulation times N_{test} of every data point are more than 100. It is found that the connection probability P_C changes consistently with the stabilization fraction F_S, and is hardly affected by CNT diameter or length. Therefore, the stabilization fraction F_S proposed in this paper can reflect very well the formation of load-transfer path in networks. When the stabilization fraction F_S is 99%, P_C is also about 99%, which means most distributions of the CNT networks can carry load. Thus the second feature of stiffness threshold can be satisfied at $F_S^C = 99\%$.

From above, it is found that the criterion of stabilization fraction $F_S^C = 99\%$ is suitable for the prediction of the stiffness threshold $\hat{\rho}_{th}^{S1}$.

3. The bending–stretching transitional threshold

For a network with load carrying capacity, the load is transferred by the deformation of CNTs. Thus the deformation modes of CNTs have significant influence on the efficiency of load transfer. For bending deformation mode, the strain distribution in CNTs is not uniform, which results in waste of materials. While for stretching deformation mode, the strain in CNTs distributes more uniformly, leading to an efficient utilization of materials. Therefore, stretching dominated deformation can transfer load more efficiently than bending, and thus leads to higher stiffness of networks, especially for the networks constructed by CNTs with large aspect ratio. Adding new CNTs into a network leads to increasing intersections between CNTs, which can restrict bending deformation and thus utilize CNTs more efficiently. Hence there is a critical point at which the main deformation mode changes from bending dominated deformation to stretching dominated deformation, as diagramed in Fig. 1. At this critical points, the relative network densities is defined as the bending–stretching transitional threshold, denoted as $\hat{\rho}_{th}^{S2}$.

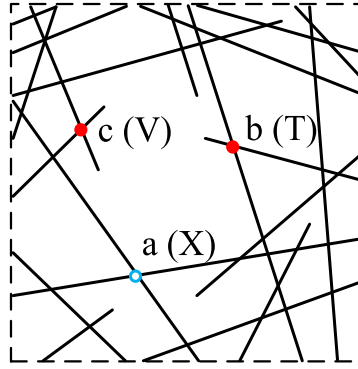This transition behavior has been found in cellular materials, in which the deformation form and mechanical properties

Fig. 6. Schematic of different types of intersections: (a) "X" type intersection, (b) "T" type intersection, and (c) "V" type intersection. The "T" and "V" types of intersections are considered as the defects of networks.

are affected by morphological imperfections (Chen et al., 1999; Grenestedt, 1998; Jin et al., 2014): the imperfection of waved cell struts can reduce stiffness distinctly (Grenestedt, 1998), and the imperfection of fractured cell walls produces the largest knock-down on the stiffness and yield strength of 2D foams (Chen et al., 1999; Jin et al., 2014). Similarly, in CNT networks, the limited length of CNTs leads to natural defects similar to fractured cell walls. Combining with the concept of "edge connectivity" (Deshpande et al., 2001; Gibson and Ashby, 1999), a new definition of defect is proposed in this paper to describe the topological features of CNT networks. Correspondingly, a concept of "defect fraction" is put forward to interpret the deformation modes of CNTs quantitatively.

3.1. Theoretical model for bending–stretching transitional threshold

3.1.1. Defect and defect fraction

In a network, two crossing CNTs can transfer loads from one to another through interactions in the overlap area between them, such as nano-welding junctions, chemical bonds and van der Waals interactions, which are all sensitive to the distance and much stronger than the interactions of other parts of CNTs. These intersections connect individual CNTs together to form a network that can carry load. Meanwhile, they divide CNTs into segments. Of all the segments, two ends of each CNT cannot devote to load transfer, and can be eliminated. Therefore the intersections in the whole network can be classified into three types according to the topology of the four linked CNT segments, assuming that all the CNTs are stable, which is reasonable for $\hat{\rho} > \hat{\rho}_{th}^{S1}$.

1. "X" type intersection: same as point (a) in Fig. 6, none of the segments is end part, which means all the four CNT segments at the intersection can carry and transfer load. The "edge connectivity" for the "X" type intersections is 4.
2. "T" type intersection: same as point (b) in Fig. 6, one segment is end part, and three of the four segments at the intersection can carry and transfer load. The "edge connectivity" for the "T" type intersections is 3.
3. "V" type intersection: same as point (c) in Fig. 6, two of the segments are end parts, and only two of the four segments at the intersection can carry and transfer load. The "edge connectivity" for the "V" type intersections is 2.

At the "T" and "V" types of intersections, the end parts that cannot carry and transfer load can be considered as fractured walls of the cells. So the "T" and "V" types of intersections are defined as the defects of networks. If the length of CNTs is unlimited relative to the network size, all the intersections can only be "X" type, and the network has no defect. However, in the bulk productions, the ratio of CNT length to the network size is less than 10^{-2}. There must be "T" and "V" type intersections due to the limited CNT length, resulting in natural defect of the network.

Suppose the total number of intersections in the network is N_{int}^{Tot} and the number of defect intersections, which is the total number of "T" and "V" types of intersections, is N_{int}^{D}. The defect fraction can then be defined as

$$F_D = N_{int}^{D}/N_{int}^{Tot}. \tag{3.1}$$

The condition to form an "X" type intersection is that this intersection does not belong to the end segments of CNTs (i.e. cannot be the first or last intersection of the CNTs). Given the average intersection number of one CNT is $\bar{N}_{int}$, according to Eq. (C.11), the probability of a CNT with i intersections is $(\bar{N}_{int}^{i} e^{-\bar{N}_{int}})/(i!)$, and among the i intersections, only $(i-2)$ intersections are possible to form "X" type intersections. Then the probability to form an "X" type intersection is

$$p_X = \sum_{i=2}^{(N_{CNT}-1)} \sum_{j=2}^{(N_{CNT}-1)} \left[\left(\frac{\bar{N}_{int}^{i} e^{-\bar{N}_{int}}}{i!} \frac{i-2}{i} \right) \left(\frac{\bar{N}_{int}^{j} e^{-\bar{N}_{int}}}{j!} \frac{j-2}{j} \right) \right]. \tag{3.2}$$

Then the defect fraction can be written as

$$F_D = 1 - p_X = 1 - \sum_{i=2}^{(N_{CNT}-1)} \sum_{j=2}^{(N_{CNT}-1)} \left[\left(\frac{\bar{N}_{int}^i e^{-\bar{N}_{int}}}{i!} \frac{i-2}{i} \right) \left(\frac{\bar{N}_{int}^j e^{-\bar{N}_{int}}}{j!} \frac{j-2}{j} \right) \right]. \tag{3.3}$$

For $\bar{N}_{int} \gg 1$, Eq. (3.3) can be simplified as

$$F_D \approx \frac{4}{\bar{N}_{int}}. \tag{3.4}$$

The difference between Eqs. (3.4) and (3.3) is only 3.7% for $\bar{N}_{int} = 6$, and as small as 0.085% for $\bar{N}_{int} = 10$.

Both Eqs. (3.3) and (3.4) show that the defect fraction F_D decreases from 100% to almost zero with the increase of average intersection number $\bar{N}_{int}$ of the networks. According to the relation between $\bar{N}_{int}$ and $\hat{\rho}$ in Eq. (2.10), the defect fraction for 2D networks is also expressed as

$$F_D = \frac{2\pi}{\hat{\rho} \lambda_{CNT}}. \tag{3.5}$$

For the networks with the same CNT aspect ratio λ_{CNT}, the defect fraction F_D also decreases with the increase of the relative density of the networks $\hat{\rho}$, as shown in Fig. 4(c) for networks with $\lambda_{CNT} = 400$.

3.1.2. Influence of defect fraction on network deformation mode

The defective intersections, i.e. the "T" and "V" types of intersections, cannot achieve equilibrium without shear stress or bending moment when load is transferred through them, as demonstrated in Fig. 7(b) and (c). So the bending deformation of the CNT segments connected at the defective intersections is inevitable. Moreover, these defective intersections can also affect the deformation mode of the segments in adjacent zones.

Therefore, the "X" type intersection is the only type of intersection that is possible to achieve equilibrium without bending deformation in the networks, because the load can be transferred along the axial direction of CNTs, as illustrated in Fig. 7(a). Especially, all the intersections could be "X" type if CNT length was unlimited. In this special case, the load can be applied to the end of CNTs when the network is analyzed using a unit cell, bending can be suppressed, and the deformation is completely stretching, exactly the same as the model proposed by Cox (1952).

In order to measure the contribution of CNT axial strain (i.e. stretching deformation) to the total deformation of network, a stretching coefficient is established as below. When an average strain ε_{11} is applied to the network, and the strain energy of the system W_{total} is $\frac{1}{2} E_N A_N (\varepsilon_{11})^2 L_1$, in which E_N is the modulus of CNT network along direction 1, and A_N is the corresponding cross section area of network. The local strain along the axial direction of each CNT segment is ε'_{11}, and the strain energy caused by stretching is $W_{stretch} = \frac{1}{2} \sum E_{CNT} A_{CNT} (\varepsilon'_{11})^2 l_{seg}$, in which E_{CNT} and A_{CNT} are the axial Young's modulus and cross section area of CNTs, respectively, and l_{seg} is the length of CNT segment. Then, based on the ratio of strain energies, the stretching coefficient $\hat{W}_{stretch}$ can be defined to interpret the degree of stretching deformation of the whole networks quantitatively as

$$\hat{W}_{stretch} = \frac{W_{stretch}}{W_{total}} = \frac{\sum E_{CNT} A_{CNT} (\varepsilon'_{11})^2 l_{seg}}{E_N A_N (\varepsilon_{11})^2 L_1}. \tag{3.6}$$

Fig. 8(a) shows the curve of the stretching coefficient $\hat{W}_{stretch}$ versus the defect fraction for the networks with $\lambda_{CNT} = 400$, 600, 800, 1200 and 1600, in which $\hat{W}_{stretch}$ is calculated from the results of FEM simulations (see Appendix D for details). With the decrease of defect fraction, the stretching coefficient $\hat{W}_{stretch}$ increases, which implies that the networks with less defect fraction F_D have higher load transfer efficiency. Therefore, with the increase in network density, the defect fraction decreases and the dominated deformation mode of CNTs changes from bending to stretching.

However, $\hat{W}_{stretch}$ depends not only on the defect fraction F_D, but also on the CNT aspect ratio λ_{CNT}, as presented in Fig. 8

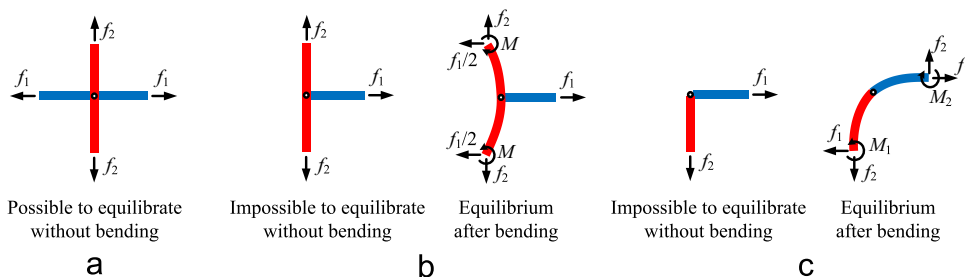| Possible to equilibrate without bending | Impossible to equilibrate without bending | Equilibrium after bending | Impossible to equilibrate without bending | Equilibrium after bending |

a   b   c

Fig. 7. Equilibrium of the three types of intersections under axial forces along both CNTs: (a) "X" type intersection, which is possible to achieve equilibrium without bending deformation; (b) "T" type intersection and (c) "V" type intersection, which are impossible to achieve equilibrium without bending deformation.
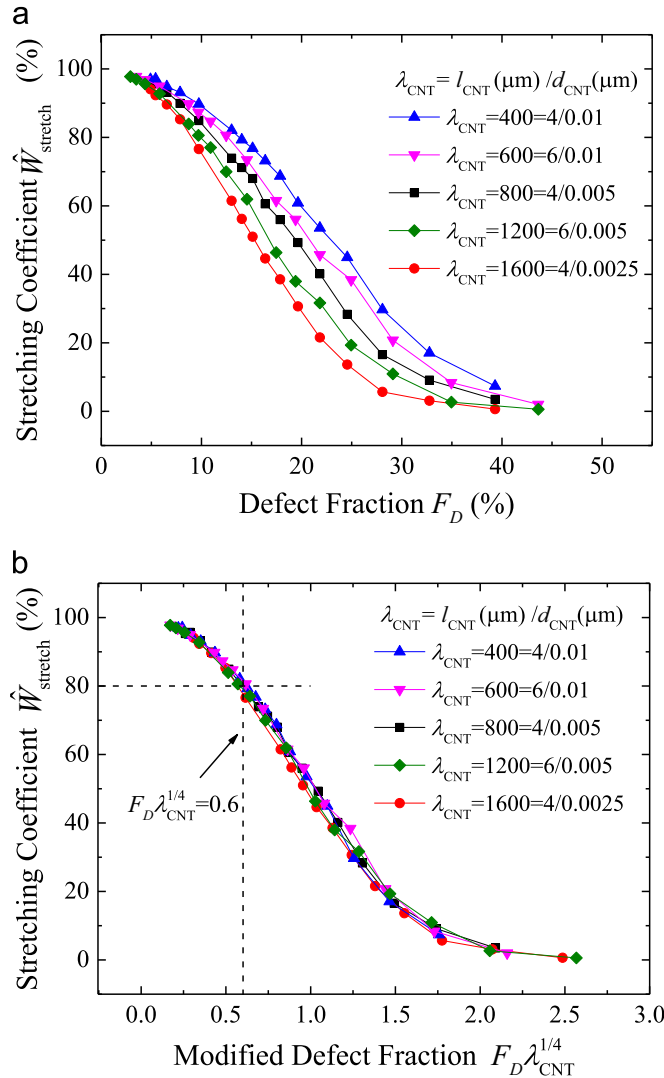
Fig. 8. The stretching coefficient versus (a) defect fraction F_D and (b) modified defect fraction $F_D\lambda_{CNT}^{1/4}$, for 2D CNT networks with different CNT lengths and diameters.

(a). As we know, for CNTs simplified as beam models, the bending stiffness is proportional to d_{CNT}^4, while the tensile stiffness is proportional to d_{CNT}^2. So for the networks with the same F_D, smaller CNT aspect ratio leads to stronger ability to resist bending deformation, and accordingly higher stretching coefficient $\hat{W}_{stretch}$. It is revealed from the simulation results that the stretching coefficient $\hat{W}_{stretch}$ can be determined by a combined parameter $F_D\lambda_{CNT}^v$ only. And when $v = 1/4$, the curves in Fig. 8 (a) converge to a single master curve, as shown in Fig. 8(b). The exponent $v = 1/4$ also consists with the study of Head et al. (2003) on the deformation of polymer networks.

As presented in Eq. (3.3) (i.e. Fig. 4(c) for networks with $\lambda_{CNT} = 400$), when the relative network density $\hat{\rho}$ is slightly higher than (but very close to) the stiffness threshold $\hat{\rho}_{th}^{S1}$ (which is 2.05% for networks with $\lambda_{CNT} = 400$), the combined defect parameter $F_D\lambda_{CNT}^{1/4}$ is over 3.0, and the strain energy caused by stretching is lower than 10% according to Fig. 8. When $F_D\lambda_{CNT}^{1/4}$ is lower than 0.6, more than 80% of the deformation energy is caused by stretch.

3.1.3. Predicting bending–stretching transitional threshold by defect fraction

According to the stretching coefficient $\hat{W}_{stretch}$, a critical value can be defined to describe the critical density as

$$\left(F_D\lambda_{CNT}^{1/4}\right)\Big|_{Critical} = C. \tag{3.7}$$

From Eqs.(3.5) and (3.7), the critical density can be estimated as

$$\hat{\rho}_{th}^{S2} = \frac{2\pi}{C} \lambda_{CNT}^{-3/4}.$$

(3.8)

Here the critical value is taken as

$$C = \left(F_D \lambda_{CNT}^{1/4} \right)\Big|_{\hat{W}_{stretch}=80\%} = 0.6,$$

(3.9)

and the critical density is then obtained from Eq. (3.8) as

$$\hat{\rho}_{th}^{S2} = \frac{10.5}{\lambda_{CNT}^{3/4}}.$$

(3.10)

Similar to $\hat{\rho}_{th}^{S1}$, the critical density $\hat{\rho}_{th}^{S2}$ can also be estimated by the average intersection number on each CNT by substituting Eq. (3.4) into Eq. (3.9)

$$\bar{N}_{int}\big|_{\hat{\rho}_{th}^{S2}} = 6.7 \lambda_{CNT}^{1/4}.$$

(3.11)

Hence the combined parameter $\bar{N}_{int} \lambda_{CNT}^{-1/4}$ can be considered as an invariant to predict the critical network density $\hat{\rho}_{th}^{S2}$, and for 2D CNT networks, it satisfies

$$\bar{N}_{int} \lambda_{CNT}^{-1/4} = 6.7 \quad \text{when} \quad \hat{\rho} = \hat{\rho}_{th}^{S2}.$$

(3.12)

3.2. Numerical validation

According to the results of FEM simulation, the bending–stretching transitional threshold can be obtained from the whole range behavior of network stiffness versus relative density, with details in Section 4.2.1.

For the network with $l_{CNT} = 4$ μm and $d_{CNT} = 0.01$ μm, Fig. 4(c) shows the defect fraction versus relative density of CNT networks as well as the critical defect fraction $F_D^C = 0.6 \lambda_{CNT}^{-1/4}$. A comparison between the FEM results in Fig. 4(a) and the

Table 2
Simulation results on stiffness parameters of 2D CNT networks with different CNT lengths and diameters.

| l_{CNT} (μm)	$d_{CNT} = 0.01$ μm			$d_{CNT} = 0.005$ μm			$d_{CNT} = 0.0025$ μm		
	$\hat{\rho}_{th}^{S2}$ (FEM)	$\hat{\rho}_{th}^{S2}$ (Theory)	k	$\hat{\rho}_{th}^{S2}$ (FEM)	$\hat{\rho}_{th}^{S2}$ (Theory)	k	$\hat{\rho}_{th}^{S2}$ (FEM)	$\hat{\rho}_{th}^{S2}$ (Theory)	k
2	0.196	0.197	0.271	0.119	0.117	0.266	0.0728	0.0698	0.246
3	0.142	0.146	0.277	0.0856	0.0866	0.276	0.0527	0.0515	0.281
4	0.116	0.117	0.273	0.0690	0.0698	0.277	0.0422	0.0415	0.279
5	0.0994	0.0993	0.272	0.0598	0.0590	0.274	0.0365	0.0351	0.275
6	0.0898	0.0866	0.269	0.0525	0.0515	0.271	0.0312	0.0306	0.275
7	0.0801	0.0772	0.269	0.0484	0.0459	0.272	0.0283	0.0273	0.275
8	0.0714	0.0698	0.272	0.0443	0.0415	0.271	0.0271	0.0247	0.271
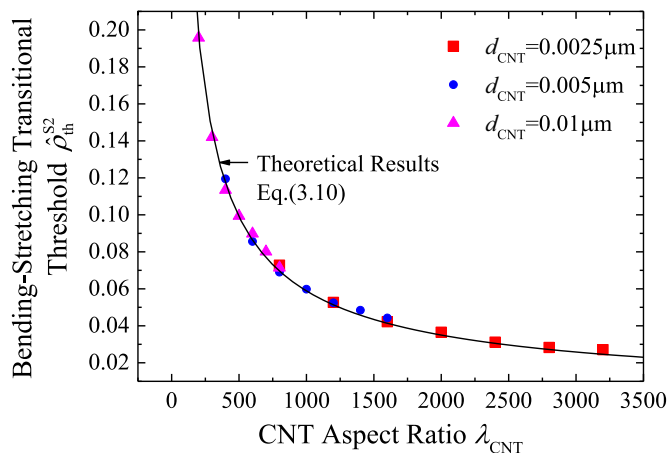
Fig. 9. Comparison between theoretical and simulation results of the critical density for 2D networks with different CNT diameters.

theoretical prediction on the bending–stretching transitional threshold presented in Fig. 4(c) illustrates that the criterion of defect fraction $F_D^C = 0.6\lambda_{CNT}^{-1/4}$ can predict the transitional threshold $\hat{\rho}_{th}^{S2}$ accurately.

Besides, the FEM simulation results of the transitional thresholds $\hat{\rho}_{th}^{S2}$ for different networks as well as the theoretical predictions by Eq. (3.10) are listed in Table 2. It is found that the theoretical results agree well with the numerical outcomes. And the stiffness threshold $\hat{\rho}_{th}^{S2}$ decreases with increasing CNT length l_{CNT} and decreasing CNT diameter d_{CNT}. The stiffness threshold $\hat{\rho}_{th}^{S2}$ for networks with different l_{CNT} and d_{CNT} are also shown in Fig. 9. It can be found that $\hat{\rho}_{th}^{S2}$ depends only on the CNT aspect ratio λ_{CNT}. As presented in Fig. 9, the stiffness threshold $\hat{\rho}_{th}^{S2}$ decreases with the increase of λ_{CNT}, and shows good agreements with the theoretical estimate of Eq. (3.10).

Therefore, the criterion established by defect fraction for the prediction of the bending–stretching transitional threshold $\hat{\rho}_{th}^{S2}$ is validated.

4. Whole range stiffness and relative network density

4.1. Three stages of stiffness

According to the theoretical prediction on the two thresholds related to the stiffness, the stiffness of CNT networks can be divided into three stages, as diagramed in Fig. 1. Fig. 4(a) shows a typical curve of normalized tensile modulus versus the relative density of CNT networks, which is obtained by the numerical simulation in Appendix D. For the case presented in Fig. 4(a), the aspect ratio of CNTs is $\lambda_{CNT} = 400$, and the relative size is $\hat{L} = L_E/l_{CNT} = 2.5$. More than 30 different randomly distributed networks are generated by a pre-process code for each given network density and then simulated for the normalized tensile modulus of the network. The three-stage behavior of network stiffness can be investigated clearly in Fig. 4(a):

1. Zero stiffness stage: when the relative density is very low, less than the stiffness threshold $\hat{\rho}_{th}^{S1}$, the normalized tensile modulus $\hat{E}$ maintains zero;
2. Bending dominated stage: when the relative density $\hat{\rho}$ grows larger than $\hat{\rho}_{th}^{S1}$, the normalized tensile modulus $\hat{E}$ is no longer zero, but increases rapidly, until $\hat{\rho}$ reaches the bending–stretching transitional threshold $\hat{\rho}_{th}^{S2}$;
3. Stretching dominated stage: when the relative density $\hat{\rho}$ becomes higher than $\hat{\rho}_{th}^{S2}$, the normalized tensile modulus $\hat{E}$ increases linearly with the increase of $\hat{\rho}$.

4.2. Load and deformation analysis on different stiffness stages

The load and deformation analysis are carried out in detail to reveal the mechanism behind the behaviors of each stage.

4.2.1. Zero stiffness stage

In zero stiffness stage, the relative density of CNT networks is very low. The CNTs scatter in the network, and the path to transfer loads is rarely formed. A typical contour of CNT axial strain ε'_{11} is shown in the deformed configuration of the network with a relative density of 2% in Fig. 10(a). The tensile load is applied in direction 1 and the applied strain is $\varepsilon_{11} = 0.1\%$. Fig. 10(a) indicates the stress level is extremely low and no obvious deformation of CNTs is investigated. Therefore, in this stage, only a few CNTs can transfer loads, the networks can hardly carry load, and the stiffness is almost zero.

4.2.2. Bending dominated stage

When the relative density of CNT networks is between $\hat{\rho}_{th}^{S1}$ and $\hat{\rho}_{th}^{S2}$, the path to transfer load begins to form. A typical axial strain contour of this stage is shown in the deformed configuration of the network with a relative density of 8% in Fig. 10(b). The load-transfer paths can be seen clearly along the loading direction (direction 1), and in these paths, the bending deformation of CNTs can be observed clearly. Therefore, in this stage, some load-transfer paths are formed, many CNTs can transfer load, and the networks have the capacity of load carrying.

However, because there are still many CNTs cannot contribute to the load carrying in the network, the stress distributes unevenly and concentrates along the paths, leading to the large bending deformations of some individual CNTs.

In this stage, the relation between the normalized tensile modulus $\hat{E}$ and the relative network density $\hat{\rho}$ reflects changes in two levels: in the whole network, the number of CNTs that constructs the load-transfer paths increases with the relative network density $\hat{\rho}$; and in each CNT, the capacity of load carrying of CNTs in networks also increases with the relative network density $\hat{\rho}$.

From the simulation results, it can be observed that the stretching coefficient $\hat{W}_{stretch}$ is approximately proportional to the relative network density $\hat{\rho}$, as shown in Fig. 11(a). So we have

$$\hat{W}_{stretch} \propto \hat{\rho}. \tag{4.1}$$

Investigating the axial strain of each CNT, it is found that the normalized average axial strain of CNTs, i.e. the ratio of the
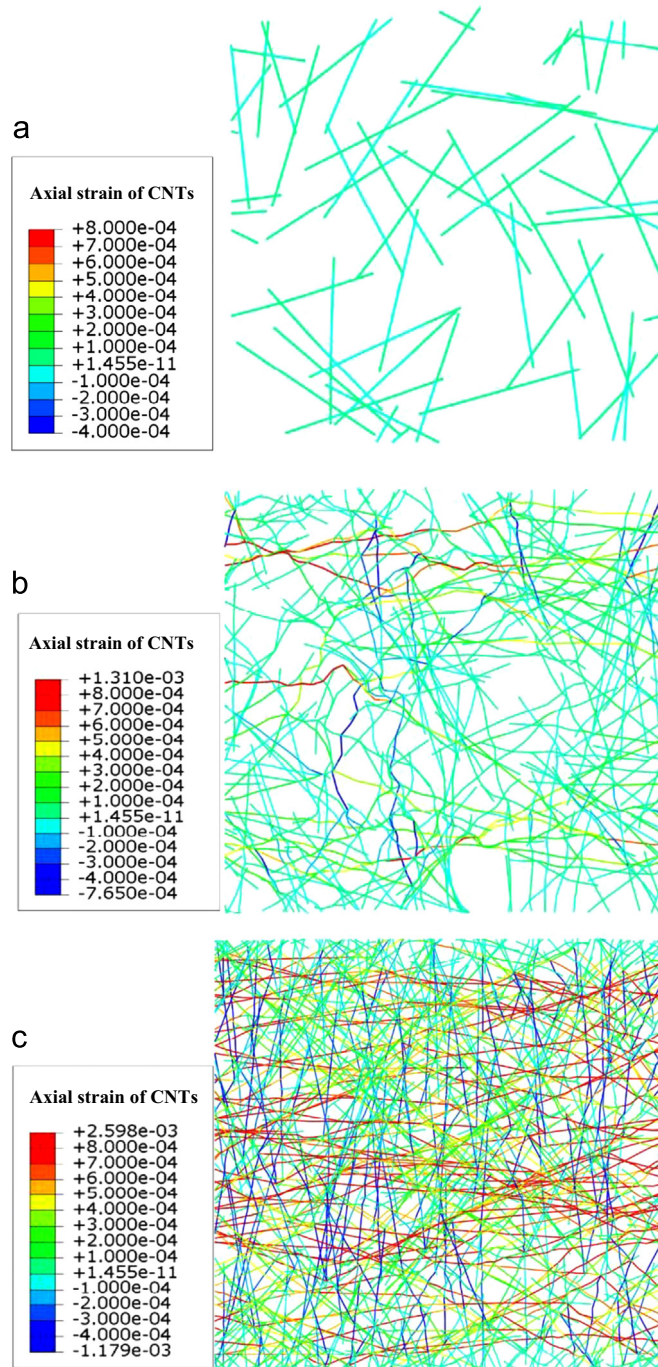
Fig. 10. Axial strain contours of CNTs and deformed configurations of networks in different stages (the network is stretched along horizontal direction): (a) zero stiffness stage ($\hat{\rho} = 2\%$), (b) transition stage ($\hat{\rho} = 8\%$), and (c) linear stage ($\hat{\rho} = 20\%$).

average magnitude of CNT axial strain $\overline{|\varepsilon'_{11}|}$ to the overall tensile strain ε_{11} of network is proportional to the relative network density $\hat{\rho}$, as shown in Fig. 11(b). Thus we have

$$\frac{\overline{|\varepsilon'_{11}|}}{\varepsilon_{11}} = \frac{\sqrt{\frac{\sum(\varepsilon'_{11})^2 l_{seg}}{N_{CNT} l_{CNT}}}}{\varepsilon_{11}} \propto \hat{\rho}. \tag{4.2}$$

Substituting Eqs. (4.1) and (4.2) into Eq. (3.6), the relation between the normalized tensile modulus $\hat{E}$ and the relative
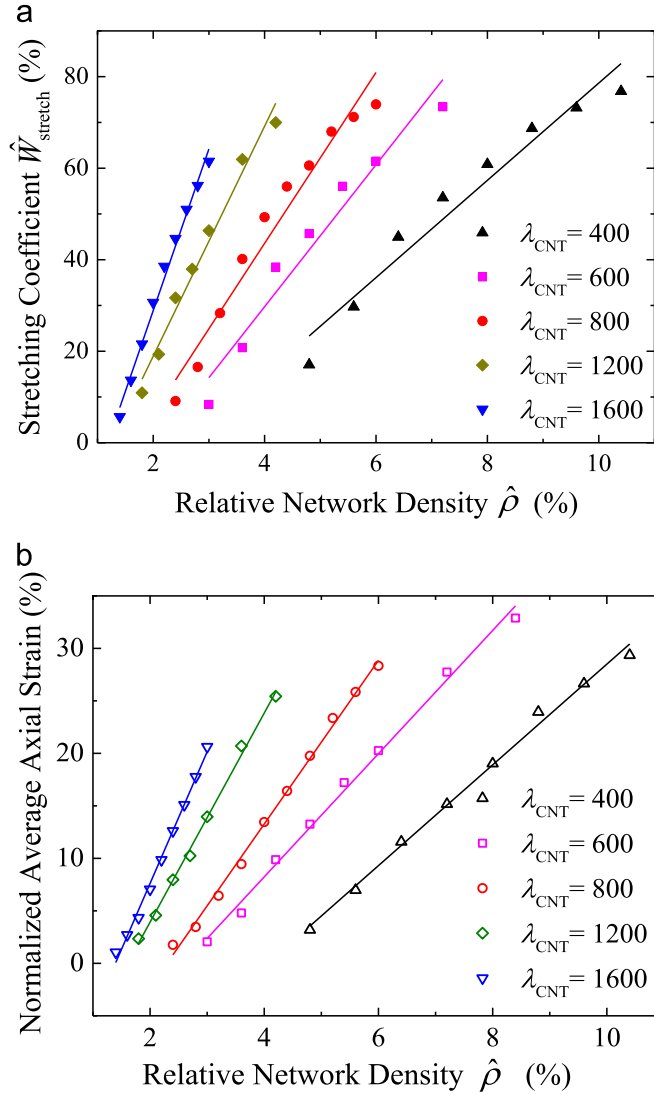
a

b

Fig. 11. The relation between deformation and relative density at the transition stage: (a) the stretching coefficient increases linearly with relative density, and (b) the average axial strain of CNT segments increases linearly with relative density.

network density $\hat{\rho}$ is obtained as

$$\hat{E} = \frac{E_N}{E_{CNT}} \propto \hat{\rho}^2. \tag{4.3}$$

This quadratic relation in Eq. (4.3) is consistent with the classic formula derived by Gibson and Ashby (1999) for the cellular solids with bending dominated strut deformation, which have the similar microstructures to the CNT networks.

4.2.3. Stretching dominated stage

When the relative density of CNT networks is higher than $\hat{\rho}_{th}^{S2}$, almost all CNTs contribute to form the load-transfer paths. A typical axial strain contour of the stretching dominated stage is shown in the deformed configuration of the network with a relative density of 20% in Fig. 10(c). It can be seen clearly in Fig. 10(c) that the main deformation mode of CNTs is stretching, rather than bending. Therefore, in this stage, plenty of load-transfer paths are formed, almost all CNTs can transfer load, and the networks have linearly increasing capacity of load carrying with increase of the relative density. The slope of the $\hat{\rho} - \hat{E}$ curve in this stage is denoted by k.

The simulation results of the slope k for the networks with various CNT lengths and diameters are listed in Table 2. It can be found that the slope k of the linear stage only changes slightly, which indicates that effect of CNT length and CNT diameter on the slope k is negligible.

This linear behavior can also be explained by classic theory of cellular solids, but Eq. (4.3) is no longer suitable due to different deformation modes. Cox (1952) has derived the linear relation between the normalized modulus and relative density of isotropic planar mat of long fibers when the dominated deformation is tensile, expressed as

$$\hat{E} = \frac{\pi}{12}\hat{\rho}. \tag{4.4}$$

Eq. (4.4) indicates that the linear relation between the normalized stiffness and relative density for the tensile (or compressive) dominated deformation of cellular materials. Therefore, it is suggested to take $k = \pi/12$ according to Cox's result (1952), which is very close to the mean value of FEM simulations, which is 0.272.

The difference between classic theory, Eqs. (4.3) and (4.4), and our theory is the stiffness thresholds $\hat{\rho}_{th}^{S1}$ and $\hat{\rho}_{th}^{S2}$. In cellular material and foams, the thresholds can be ignored due to their high relative density and small aspect ratio of struts (Jin et al., 2013), but they are important for CNT networks, which may have a very low relative density.

4.3. Whole range stiffness prediction

From the above observation and analysis, the normalized modulus remains zero in the first stage, then increases quadratically and linearly with relative density in the second and third stages, respectively. Considering the continuity between stages, the $\hat{\rho} - \hat{E}$ curve can be expressed by the piecewise function as

$$\hat{E} = \begin{cases} 0, & 0 < \hat{\rho} \leq \hat{\rho}_{th}^{S1}, \\ \dfrac{k\left(\hat{\rho} - \hat{\rho}_{th}^{S1}\right)^2}{2\left(\hat{\rho}_{th}^{S2} - \hat{\rho}_{th}^{S1}\right)}, & \hat{\rho}_{th}^{S1} < \hat{\rho} < \hat{\rho}_{th}^{S2}, \\ k\left(\hat{\rho} - \dfrac{\hat{\rho}_{th}^{S1} + \hat{\rho}_{th}^{S2}}{2}\right), & \hat{\rho} \geq \hat{\rho}_{th}^{S2}. \end{cases} \tag{4.5}$$

Eq. (4.5) indicates that the relation between stiffness and density of the CNT networks, i.e. $\hat{\rho} - \hat{E}$ curve, depends only on three parameters, the thresholds $\hat{\rho}_{th}^{S1}$ and $\hat{\rho}_{th}^{S2}$, and the slope of stretching dominated stage k. The stiffness threshold $\hat{\rho}_{th}^{S1}$ is obtained by the criterion of stabilization fraction $F_S = 99\%$. The bending–stretching transitional threshold $\hat{\rho}_{th}^{S2}$ and slope k can be obtained by fitting the FEM simulation data using the third expression in Eq. (4.5), i.e. $\hat{E} = k\left[\hat{\rho} - \left(\hat{\rho}_{th}^{S1} + \hat{\rho}_{th}^{S2}\right)/2\right]$. In the fitting process, the data points are reduced one by one from lower network density to higher network density, until the linearly dependent coefficient is greater than 0.999. Thus $\hat{\rho}_{th}^{S2}$ and k are obtained.

For the case shown in Fig. 4(a), we have the slope $k = 0.273$, the thresholds $\hat{\rho}_{th}^{S1} = 2.05\%$ and $\hat{\rho}_{th}^{S2} = 11.6\%$. The $\hat{\rho} - \hat{E}$ curve is fitted using Eq. (4.5) as

$$\hat{E}\Big|_{\substack{l_{CNT} = 4\,\mu m \\ d_{CNT} = 0.01\,\mu m}} = \begin{cases} 0, & 0 < \hat{\rho} \leq 2.05\%, \\ 1.43\left(\hat{\rho} - 2.05\%\right)^2, & 2.05\% < \hat{\rho} < 11.6\%, \\ 0.273\left(\hat{\rho} - 6.83\%\right), & \hat{\rho} \geq 11.6\%. \end{cases} \tag{4.6}$$

Based on the theoretical analysis of Sections 2 and 3, the thresholds $\hat{\rho}_{th}^{S1}$ and $\hat{\rho}_{th}^{S2}$ depends only on the CNT aspect ratio λ_{CNT}, as revealed by Eqs. (2.8) and (3.10). And the constant slope k is about $\pi/12$ for 2D networks according to Cox's result (1952). Thus, the $\hat{\rho} - \hat{E}$ relation depends only on the CNT aspect ratio λ_{CNT}, and a simple expression to estimate the network stiffness can be established from Eqs. (2.8), (3.10) and (4.5), expressed as

$$\hat{E} = \begin{cases} 0, & 0 < \hat{\rho} \leq \dfrac{8.2}{\lambda_{CNT}}, \\ \dfrac{\pi\lambda_{CNT}}{251.3\lambda_{CNT}^{1/4} - 197.2}\left(\hat{\rho} - \dfrac{8.2}{\lambda_{CNT}}\right)^2, & \dfrac{8.2}{\lambda_{CNT}} < \hat{\rho} < \dfrac{10.5}{\lambda_{CNT}^{3/4}}, \\ \dfrac{\pi}{12}\left(\hat{\rho} - \dfrac{10.5\lambda_{CNT}^{1/4} + 8.2}{2\lambda_{CNT}}\right), & \hat{\rho} \geq \dfrac{10.5}{\lambda_{CNT}^{3/4}}. \end{cases} \tag{4.7}$$

4.4. Discussions

CNTs are easily curved in the networks due to the van der Waals interactions and thermal fluctuations. The curliness of CNTs may degrade the mechanical and electrical properties of the whole network (Berhan et al., 2004a; Li et al., 2008; Lu et al., 2010; Ma and Gao, 2008; Yi et al., 2004). Therefore, the influence of CNT curliness on the stiffness and thresholds of
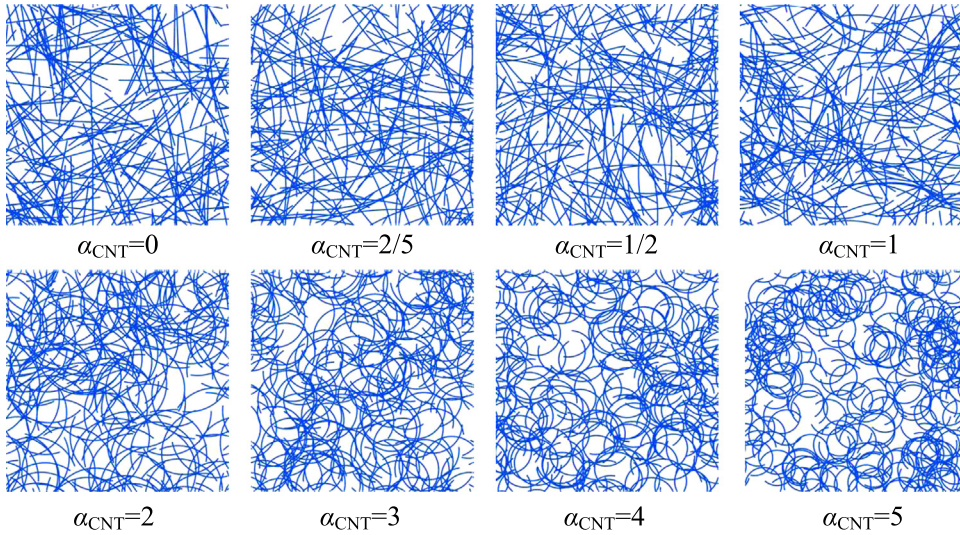
Fig. 12. Schematic diagram of CNT networks with different CNT radian α_{CNT}.

networks is discussed briefly below.

Assuming all the CNTs in the network are curved along an arc with the curvature radius R_{CNT}, the radian of the arc can be expressed as

$$\alpha_{CNT} = l_{CNT}/R_{CNT}. \tag{4.8}$$

The radian α_{CNT} is used here to quantify the curliness of CNTs, and the CNTs are curved severely if α_{CNT} is large.

Fig. 12 presents the networks with the same CNT density ($n_{CNT}=2$) but different radian α_{CNT}. The size of RVE and the length of CNTs are $L_E=10$ μm and $l_{CNT}=4$ μm, respectively. When $\alpha_{CNT}=0$, the CNTs are straight, same as the model built in Fig. 3. Using the same FEM simulation and statistical analysis method as developed in Section 2.2.2, the connection probability of load-transfer path P_C (defined in Eq. (2.14)) and the tensile modulus of the networks can be obtained with respect to the network density, as shown in Fig. 13(a) and (b), respectively.

It can be found from Fig. 13(a) that the connection probability of load-transfer path in networks with curved CNTs is very close to that with straight CNTs when α_{CNT} is small enough ($\alpha_{CNT} \leq 2$), indicating the applicability of straight-CNT model for the networks with slightly curved CNTs. The curliness effect on the network stiffness and the bending–stretching transitional threshold $\hat{\rho}_{th}^{S2}$ can be observed from the $\hat{\rho} - \hat{E}$ curves in Fig. 13(b). The stiffness of networks with different α_{CNT} all presents three-stage behavior, but only the $\hat{\rho} - \hat{E}$ curves of networks with small radian ($\alpha_{CNT} \leq 1$) agree well with the straight-CNT model, indicating that the method and conclusions of straight-CNT model are applicable for the networks with slightly curved CNTs ($\alpha_{CNT} \leq 1$). For the networks with significantly curved CNTs, especially for those with $\alpha_{CNT} \geq 2$, the $\hat{\rho} - \hat{E}$ curves move to the right obviously, indicating a significant increase in $\hat{\rho}_{th}^{S2}$, but the slope k of linear stage of the $\hat{\rho} - \hat{E}$ curve remains almost unchanged.

Fig. 14 exhibits the influence of CNT curliness on the stiffness threshold $\hat{\rho}_{th}^{S1}$ and the bending–stretching transitional threshold $\hat{\rho}_{th}^{S2}$. It can be found that both $\hat{\rho}_{th}^{S1}$ and $\hat{\rho}_{th}^{S2}$ increases with the increase of radian α_{CNT}, and $\hat{\rho}_{th}^{S2}$ increases faster than $\hat{\rho}_{th}^{S1}$. Therefore, from Fig. 14, the two thresholds for the networks with curved CNTs can be estimated by the fitted expressions below.

$$\hat{\rho}_{th}^{S1} = \left(1 + 0.0448\alpha_{CNT} + 0.0222\alpha_{CNT}^2 \right)\hat{\rho}_{th}^{S1}|_{\alpha_{CNT}=0}, \tag{4.9}$$

$$\hat{\rho}_{th}^{S2} = \left(1 + 0.388\alpha_{CNT} \right)\hat{\rho}_{th}^{S2}|_{\alpha_{CNT}=0}. \tag{4.10}$$

It should be noted that researchers are trying to make the CNTs in the networks as straight as possible (Lu and Chen, 2010; Oh et al., 2015; Wang et al., 2010). For example, Oh et al. (2015) reported an easy preparation of CNT networks constructed by slightly curved CNTs ($\alpha_{CNT} < 0.6$), and in this case, the straight-CNT model and its results are applicable.

5. Stiffness and stiffness thresholds of 3D CNT networks

In some applications of CNT networks, such as bulk CNT composites, the 2D network model is no longer applicable. Does the stiffness of 3D CNT networks also follow the same three-stage pattern as 2D CNT networks and present two stiffness thresholds? To answer this question, the studies on the stiffness and the stiffness thresholds of 3D CNT networks are carried out in this section.
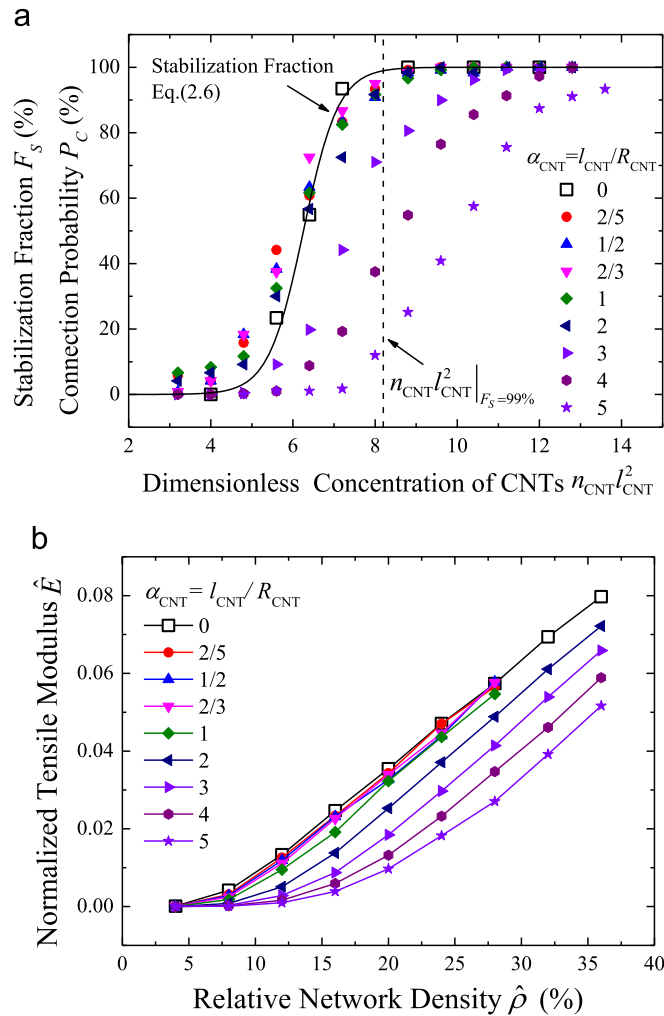
Fig. 13. Influence of CNT curliness on (a) the connection probability of load-transfer path and (b) bending–stretching transitional threshold $\hat{\rho}_{th}^{S2}$ and the slope k of the linear stage of networks.
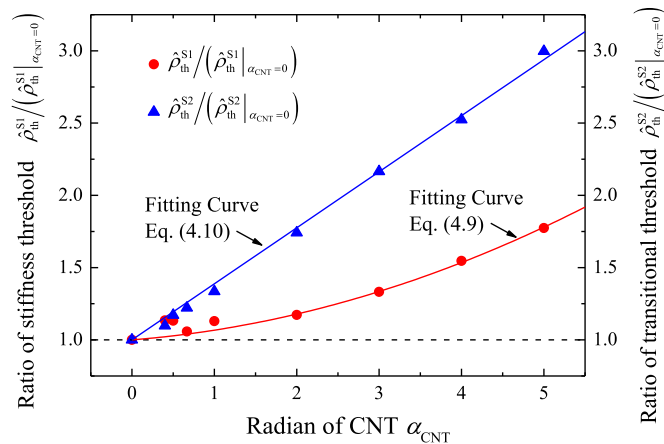

Fig. 14. Influence of CNT curliness on the stiffness threshold $\hat{\rho}_{th}^{S1}$ and the bending–stretching transitional threshold $\hat{\rho}_{th}^{S2}$ of CNT networks.

5.1. Model of 3D CNT networks

Similar to the 2D periodic unit cell, a 3D representative volume element (RVE) is set up, as shown in Fig. 15. CNTs are
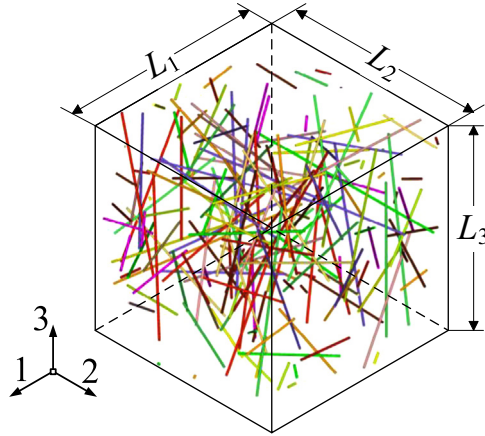
Fig. 15. A representative volume element for a 3D CNT network with periodic boundaries.

simplified as slim cylinders with the length l_{CNT} and diameter d_{CNT}, and the position and orientation of the CNT are determined by the midpoint (X_1, X_2, X_3) and the angles φ and θ. In a given cuboid of $L_1 \times L_2 \times L_3$, X_1, X_2 and X_3 follow uniform distributions in the ranges of $[0, L_1)$, $[0, L_2)$ and $[0, L_3)$, respectively. To simulate the randomly orientated CNTs, the angle θ follows an uniform distribution in the range of $[0, \pi)$, while φ follows a distribution in the range of $[0, \pi/2)$, of which the probability density function is $\sin \varphi$ (Neda et al., 1999). Meanwhile, segments beyond the cuboid zone are cut and moved to corresponding positions following the equations below:

$$x_i = \begin{cases} x_i^{old} - L_i, & x_i^{old} > L_i, \\ x_i^{old} + L_i, & x_i^{old} < 0 \qquad (i = 1, 2, 3). \\ x_i^{old}, & 0 < x_i^{old} < L_i, \end{cases}$$

(5.1)

The tensile modulus of 3D networks is normalized by the axial Young's modulus of CNT as

$$\hat{E} = \frac{E_N}{E_{CNT}} = \frac{F_1}{E_{CNT} \varepsilon_{11} L_2 L_3}.$$

(5.2)

And the relative density of 3D networks is defined as

$$\hat{\rho} = \frac{\pi N_{CNT} l_{CNT} d_{CNT}^2}{4 L_1 L_2 L_3} = \frac{\pi}{4} n_{CNT}^{3D} l_{CNT} d_{CNT}^2.$$

(5.3)

Here $n_{CNT}^{3D} = N_{CNT}/(L_1 L_2 L_3)$ is the average number of CNTs in a unit volume. $L_1 = L_2 = L_3 = L_E^{3D}$ is assumed in the following studies for the sake of simplicity.

5.2. The stiffness threshold of 3D networks

5.2.1. Prediction of stiffness threshold

For 3D CNT networks, the concept of stability should be extended to a 3D space. The triangle nucleus constructed by three interacting CNTs is no longer a stable structure in 3D space. The stable nucleus of 3D networks should be a tetrahedron-like spatial structure which consists of 6 CNTs. Therefore, the stable nucleus of 3D networks is redefined as presented in Fig. 16, following the procedures below:

1. Search for a triangle constructed by three intersecting CNTs, number the CNTs as #1, #2 and #3, and denote the triangle by △123, as shown in Fig. 16(a);
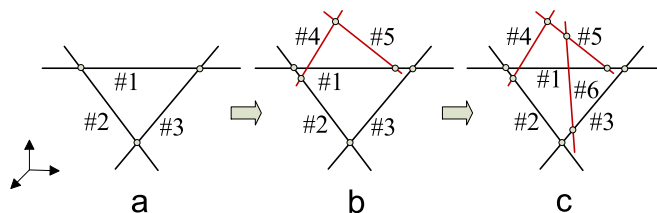

Fig. 16. Steps to build a stable nucleus for 3D CNT networks: an example.
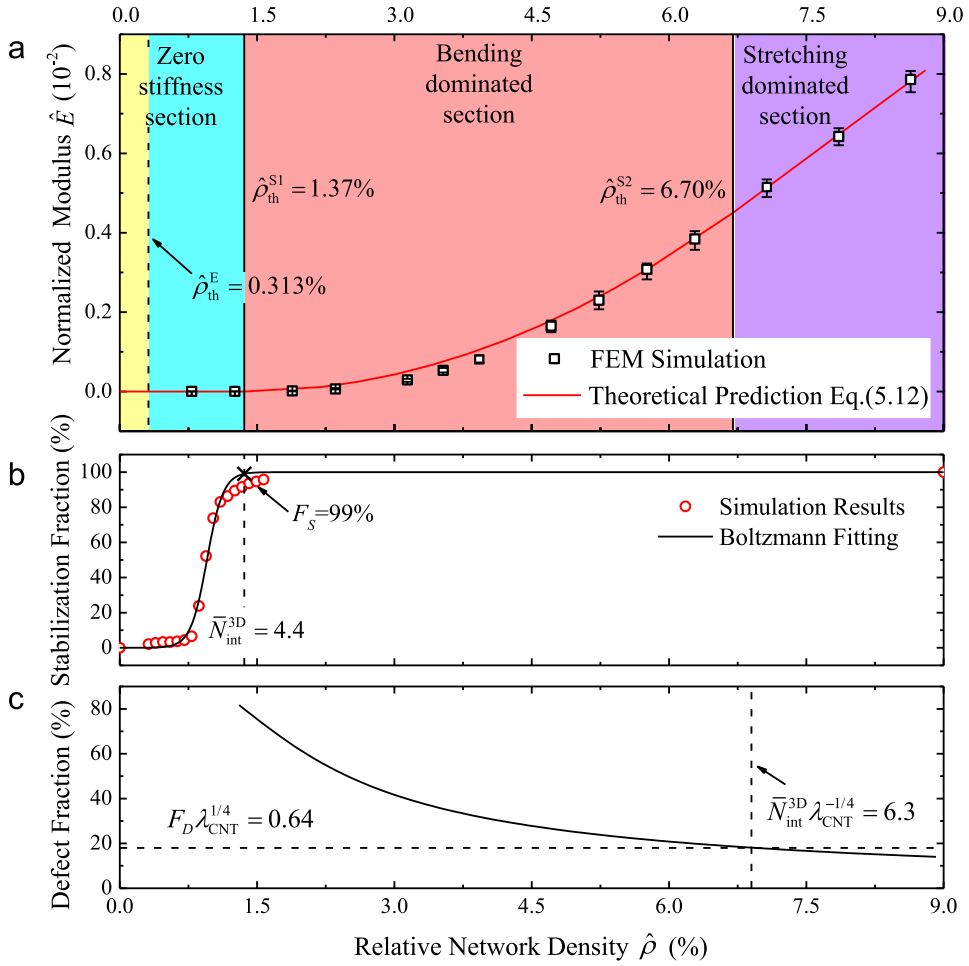
Fig. 17. Curves of (a) normalized tensile stiffness, (b) stabilization fraction, and (c) defect fraction versus the relative density of 3D networks with CNT aspect ratio $\lambda_{CNT} = 160$.

2. Search for two intersecting CNTs numbered as #4 and #5, and each of them also intersects with one of the CNTs of △123, as shown in Fig. 16(b);
3. Search for CNT #6, which intersects with either CNT #4 or #5 and one of the three CNTs of △123, and CNT #4, #5 and #6 cannot intersect with the same CNT of △123.

Thus the six CNTs construct a stable nucleus of 3D networks and all of them are considered to be stable. The CNTs intersecting with two of the stable CNTs are also considered to be stable. The stabilization fraction can then be defined by Eq. (2.1).

From the results in Section 2.2.2, the stabilization fraction of 2D networks is a monotonic function of average intersection per CNT $\bar{N}_{int}$. Similarly, for 3D CNT networks, the stabilization fraction is also dominated by the number of average intersection $\bar{N}_{int}^{3D}$. And it is proved in Appendix C that the number of intersections on a CNT in 3D network follows the same Poisson distribution as Eq. (C.12). Fig. 17(b) shows the Monte Carlo simulation results of stabilization fraction for a 3D network with the relative size $\hat{L} = L_E^{3D}/l_{CNT} = 1.25$ and the CNT aspect ratio $\lambda_{CNT} = 160$. The curve is similar to that of 2D network in Fig. 4(b), but the process of stabilizing to 100% is relatively slower. The relationship can be fitted by the Boltzmann function as

$$F_S = 1 - \frac{1}{1 + \exp\left[3.520\left(\bar{N}_{int}^{3D} - 3.046\right)\right]}. \tag{5.4}$$

Using the same criterion as 2D networks, $F_S^C = 99\%$, a universal invariant for the prediction of stiffness threshold is found for 3D CNT networks, expressed by the average intersection number using Eq. (5.4) as

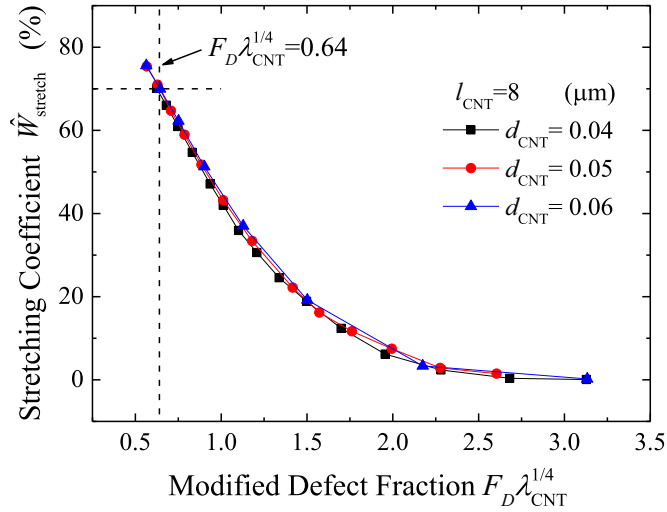$$\bar{N}_{int}^{3D}\Big|_{\hat{\rho}_{th}^{S1}} = 4.4. \tag{5.5}$$

Fig. 18. The stretching coefficient versus modified defect fraction $F_D \lambda_{CNT}^{1/4}$ for 3D networks with different CNT aspect ratios.

For 3D CNT networks, the average intersection number of each CNT is derived in Appendix C as

$$\bar{N}_{int}^{3D} = \frac{\pi}{2} l_{CNT}^2 d_{CNT} n_{CNT}^{3D}.$$
(5.6)

The relation between the relative density and the average intersection number of 3D CNT networks is then obtained from Eqs. (5.3) and (5.6) as

$$\bar{N}_{int}^{3D} = 2\lambda_{CNT} \hat{\rho}.$$
(5.7)

Therefore the stiffness threshold can be obtained from Eqs. (5.5) and (5.7) as

$$\hat{\rho}_{th}^{S1} = \frac{2.2}{\lambda_{CNT}}.$$
(5.8)

5.2.2. Numerical validation

Similar to 2D model, the numerical models for 3D CNT networks are also generated by a pre-process code. The CNTs are considered as elastic isotropic beams, and the Timoshenko beam element in space (B32) are used in the simulation with ABAQUS/Standard (2005). The interaction between two crossing CNTs at their intersection is simplified as a hinge joint. The periodic boundary conditions are applied to the RVE by constraining nodes on opposite faces of the boundary, and the rotation continuity of the boundary nodes on all the cut-and-moved CNTs is also taken into account.

Fig. 17(a) shows that the curve of normalized tensile modulus versus relative density of a 3D CNT networks with $\lambda_{CNT} = 160$. The relative size of the RVE to the CNT length is $\hat{L} = L_E^{3D}/l_{CNT} = 1.25$, and more than 20 different RVEs are generated for each network density to reach a result with low standard deviation. Fig. 17(b) shows the stabilization fraction versus relative density of CNT networks. It can be seen that the FEM results show good agreement with the prediction of Eq. (5.8), which implies that the criterion $F_S^C = 99\%$ is also proper for 3D models.

5.3. The bending–stretching transitional threshold of 3D networks

5.3.1. Prediction of the bending–stretching transitional threshold

In 3D networks, the definitions of defect and defect fraction in Section 3.1.1 are still applicable.

Fig. 18 shows the curve of the stretching coefficient $\hat{W}_{stretch}$ versus the combined defect parameter $F_D \lambda_{CNT}^{1/4}$ for the networks with $\lambda_{CNT} = 133$, 160 and 200, in which $\hat{W}_{stretch}$ is calculated from the numerical results and Eq. (3.6). It is found that all the

Table 3
Simulation results on stiffness parameters of 3D CNT networks with different aspect ratios.

λ_{CNT}	k	$\hat{\rho}_{th}^{S2}$ (FEM)	$\hat{\rho}_{th}^{S2}$ (Theory)
200	0.166	0.0551	0.0588
160	0.170	0.0670	0.0695
133	0.167	0.0790	0.0798

curves consist with each other, which indicates that the stretching coefficient $\hat{W}_{\text{stretch}}$ depends on $F_D\lambda_{\text{CNT}}^{1/4}$ only, same as the case of 2D networks.

Considering the differences in dimensions of networks as well as the simulation results of one 3D case ($\lambda_{\text{CNT}} = 160$), the critical stretching coefficient is set as $\hat{W}_{\text{stretch}}\big|_{\hat{\rho}_{\text{th}}^{S2}} = 70\%$. The critical value for the bending–stretching transitional threshold can be obtained from Fig. 18 as

$$\left(F_D\lambda_{\text{CNT}}^{1/4}\right)\Big|_{\text{Critical}} = \left(F_D\lambda_{\text{CNT}}^{1/4}\right)\Big|_{\hat{W}_{\text{stretch}}=70\%} = 0.64. \tag{5.9}$$

The threshold is then obtained from Eqs. (3.4), (5.7) and (5.9) as

$$\hat{\rho}_{\text{th}}^{S2} = \frac{3.13}{\lambda_{\text{CNT}}^{3/4}}. \tag{5.10}$$

Moreover, a universal invariant to estimate the bending–stretching transitional threshold of 3D CNT networks is obtained from Eqs.(3.4) and (5.9) as

$$\bar{N}_{\text{int}}^{3D}\lambda_{\text{CNT}}^{-1/4} = 6.3 \quad \text{when } \hat{\rho} = \hat{\rho}_{\text{th}}^{S2}. \tag{5.11}$$

5.3.2. Numerical validation

The bending–stretching transitional threshold can be obtained by the same method for the 2D model. For the example shown in Fig. 17(a), the bending–stretching threshold is $\hat{\rho}_{\text{th}}^{S2} = 6.70\%$, which shows good agreement with the predictions in Fig. 17(c). Besides, in Table 3, the simulation results of the critical density $\hat{\rho}_{\text{th}}^{S2}$ for 3D networks with $\lambda_{\text{CNT}} = 133$ and 200 also show good agreement with the theoretical estimation of Eq. (5.10), which proves that the criterion of defect fraction $F_D^C = 0.64\lambda_{\text{CNT}}^{-1/4}$ can predict the bending–stretching transitional threshold $\hat{\rho}_{\text{th}}^{S2}$ accurately.

5.4. Whole range stiffness of 3D networks

For the example shown in Fig. 17(a), the stiffness of 3D CNT networks also presents three-stage pattern: zero stage, bending dominated stage, and stretching dominated stage. Accordingly, the stiffness of 3D CNT networks can also be expressed by the piecewise function Eq. (4.5), which only depends on three parameters, the stiffness threshold $\hat{\rho}_{\text{th}}^{S1}$, the bending–stretching transitional threshold $\hat{\rho}_{\text{th}}^{S2}$ and the slope of the stretching dominated stage k.

The slope k of 3D networks is different from that in the 2D model. As shown in Fig. 17(a), $k = 0.1696$ is obtained for the 3D model with the aspect ratio $\lambda_{\text{CNT}} = 160$ using the same way as in the 2D model. The simulations for 3D networks with $\lambda_{\text{CNT}} = 133$ and 200 are also carried out, and the results are also listed in Table 3. It can be found that the values of k fit well with Christensen's result for stretching dominated 3D cellular materials, in which the normalized tensile modulus and the relative network density satisfy the expression $\hat{E}/\hat{\rho} = 1/6$ (Christensen, 1986; Christensen and Waals, 1972).

Thus, a simple expression to estimate the stiffness of 3D CNT networks can be established from Eqs. (5.8), (5.10) and (4.5) as follows:

$$\hat{E} = \begin{cases} 0, & 0 < \hat{\rho} \leq \dfrac{2.2}{\lambda_{\text{CNT}}}, \\[2mm] \dfrac{\lambda_{\text{CNT}}}{37.5\lambda_{\text{CNT}}^{1/4} - 26.1}\left(\hat{\rho} - \dfrac{2.2}{\lambda_{\text{CNT}}}\right)^2, & \dfrac{2.2}{\lambda_{\text{CNT}}} < \hat{\rho} < \dfrac{3.1}{\lambda_{\text{CNT}}^{3/4}}, \\[3mm] \dfrac{1}{6}\left(\hat{\rho} - \dfrac{3.1\lambda_{\text{CNT}}^{1/4} + 2.2}{2\lambda_{\text{CNT}}}\right), & \hat{\rho} \geq \dfrac{3.1}{\lambda_{\text{CNT}}^{3/4}}. \end{cases} \tag{5.12}$$

6. Conclusions

The properties of CNT networks may change suddenly with increasing network density, such as the sudden change in electrical conductivity at the electrical percolation threshold, which has been widely studied. This paper focuses on the sudden change in stiffness of the CNT networks and especially reveals the existence of stiffness threshold. The following conclusions on the stiffness of CNT networks are established in this paper.

(1) Both the theoretical analysis and numerical simulation identify the stiffness threshold of CNT networks, at which the stiffness increases from zero to nonvanishing suddenly. This stiffness threshold is higher than the electrical percolation threshold, and can be explained and predicted by the geometric probability analysis on the statical determinacy of CNTs in the network.
(2) The average intersection number on each CNT is revealed as an invariant at both the electrical percolation threshold and

the stiffness threshold. It is approximately 3.7 for electrical percolation threshold, and 5.2 for the stiffness threshold of 2D networks, and for 3D networks it is 1.4 and 4.4 respectively.

(3) A method to estimate the bending–stretching transitional threshold, which signs whether or not most of the CNTs in network are utilized efficiently to carry load, is developed based on the network defect analysis, and the average intersection number divided by the fourth root of CNT aspect ratio is found to be an invariant at the bending–stretching transitional threshold, which is 6.7 and 6.3 for 2D and 3D networks, respectively.

(4) A simple piecewise expression to predict the whole range of the stiffness of CNT networks, i.e. zero stiffness, bending dominated and stretching dominated stages is established, in which the relative network stiffness depends only on the relative network density and the CNT aspect ratio, which will provide great convenience for the optimum design and property prediction of CNT networks.

Acknowledgments

Appendix A. Process of Monte Carlo simulation on stabilization fractions

Given the size of the unit cell (L_E) and the length and number of CNTs (l_{CNT} and N_{CNT}) in the unit cell, the randomly distributed network can be generated and the stabilization fraction of the network can be obtained by Monte Carlo simulation following the steps below.

1. Preprocess to search stable CNTs
(1) given L_E, l_{CNT} and N_{CNT}, generate the randomly distributed CNT network;
(2) calculate the intersection relations between CNTs;
(3) establish a set for each CNT to record all the other CNTs crossing over it;
(4) sort the CNTs by their set size (i.e. the number of the intersections on them);
(5) put the CNTs with at least two intersections into a group named "free group".

2. Search for the basic stable clusters of CNTs:
2.1. Search for the nucleus of CNT triangle of in the "free group":
(1) if no CNT exists in the "free group", go to Step 3;
(2) mark the unmarked CNT with the most intersections as CNT #1;
(3) in the set of CNT #1, mark the unmarked CNT with largest set as CNT #2;
(4) in the set of CNT #2, mark the unmarked CNT with largest set as CNT #3;
(5) if CNT #3 belongs to the set of CNT #1, go to Step 2.2; otherwise, go back to Step 2.1(3) for all the unmarked CNTs;
(6) if all the CNTs in the set of CNT #2 are marked, go back to Step 2.1(2) for all the unmarked CNTs;
(7) if all the CNTs in the set of CNT #1 are marked, go back to Step 2.1(1) for all the unmarked CNTs;
(8) if all the CNTs are marked, go to Step 3.

2.2. Search for the rest stable CNTs of the cluster
(1) move the three stable CNTs of the triangle nucleus from "free group" to a group named "stable cluster(i)", and update $N_{SC}(i)$ as $N_{SC}(i)=3$;
(2) search in the "free group" to find CNTs belonging to at least two sets of CNTs in the "stable cluster(i)", or two intersected CNTs, which both have an intersection with the "stable cluster(i)", and n CNTs are found;
(3) if $n > 0$:

update $N_{SC}(i)$ as $N_{SC}(i)= N_{SC}(i)+n$;
update the clusters by moving the n CNTs from the "free group" to the "stable cluster(i)";
update $i=i+1$, and go back to Step 2.1.
(4)Otherwise, if $n=0$, update $i=i+1$, and go to Step 2.1.
3. Merge basic stable cluster
(1) pick cluster(o) and cluster(p) ($o < p$) form the "stable clusters" in orders;
(2) search intersections belong to both of the two clusters, and m_1 intersections are found;
(3) search in the "free group" to find CNTs which have intersections with both of the two clusters, and m_2 CNTs are found;
(4) search cluster(q_t) which has intersections with both of the two clusters, and m_3 cluster (q_t) are found, where $t=1,\ldots,m_3$;
(5) if one of the following conditions is established, $m_1+m_2 > 1$, $m_1+m_3 > 1$, $m_2+m_3 > 2$:
Update $N_{SC}(o)$ as $N_{SC}(o) = N_{SC}(o) + N_{SC}(p) + m_2 + \sum_t^{m_3} N_{SC}(q_t)$;
move the CNTs of cluster(p) and cluster(q_t) to cluster (o);
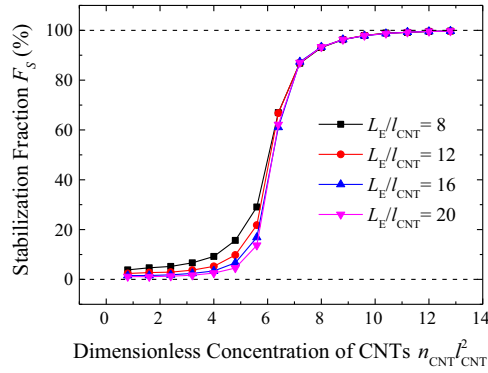delete cluster (p) and cluster (q_t) in the "stable clusters";

Fig. B1. Effect of unit cell size on the stabilization fraction of 2D CNT networks.

Table B.1
Convergence of C_0 versus different sizes of unit cell.

$\hat{L}$	C_0	$[C_0|_{\hat{L}} - C_0|_{\hat{L}-2}]/C_0|_{\hat{L}}$
8	0.37623	—
10	0.37855	0.00617
12	0.38319	0.0123
14	0.38626	0.00801
16	0.39016	0.0101
18	0.38905	−0.00284
20	0.39091	0.00478

move the m_2 CNTs from the "free group" to the cluster (o).
(6) go to Step 3(1) when no cluster can be merged.

4. Search for the CNT number of the largest "stable cluster"
set $N_{LSC} = \max\{N_{SC}(i)\}$.
5. Calculate the stabilization fraction using Eq. (2.1) as $F_S = N_{LSC}/N_{CNT}$.

Appendix B. Size effect and convergence study of stabilization fraction of 2D networks

If the size of a unit cell is not large enough relative to the CNT length, the S-shape curve is influenced by the relative size $\hat{L} = L_E/l_{CNT}$, especially for the first two stages of the curve in Fig. 2. Hence the size effect and convergence of the simulation results are necessary to be discussed here.

The S-shape curves of 2D CNT networks with different relative sizes $\hat{L} = 8, 12, 16, 20$ are shown in Fig. B1. It can be observed that the curve for networks with a higher relative size $\hat{L}$ has a lower initial platform value F_{S1} in the first stage and a shorter second stage with a sharper slope K and a higher C_0. However, the initial platform value F_{S1} converges to zero, and K and C_0 also converge with increasing $\hat{L}$.

It is important to use a proper $\hat{L}$ in the numerical simulation to eliminate the size effect and save the simulation time. Therefore, a convergence analysis is performed on the fitting parameters C_0 to determine an acceptable $\hat{L}$. Table B1 lists the Boltzmann fitting parameters C_0 as well as its convergence parameters $[C_0|_{\hat{L}} - C_0|_{\hat{L}-2}]/C_0|_{\hat{L}}$ for different $\hat{L}$. The relative size is considered large enough when $\hat{L} \geq 20$ because the convergence parameter is less than 0.5% at $\hat{L} = 20$, as listed in Table B1. The converged stabilization fraction F_S can be fitted by Boltzmann function as

$$F_S = 1 - \frac{1}{1 + \exp\left[2.3421\left(n_{CNT} l_{CNT}^2 - 6.2546 \right) \right]}.$$
(B.1)

Appendix C. Intersection probability and average intersection number

C.1 Average intersection number of 2D networks

A 2D CNT network can be modeled by randomly distributed line segments in a unit cell, as discussed in Section 2.2 and
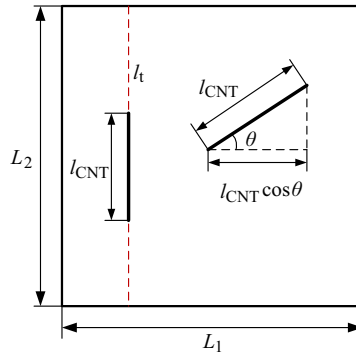
Fig. C1. Schematic diagram of the test-line method for the probability of two arbitrary in-plane CNTs intersecting with each other.

presented in Fig. 3. The CNTs interact with each other at every intersection, and the number of intersections can be estimated based on geometric probability analysis.

In a 2D network constructed by randomly distributed line segments with the length l_{CNT} much less than the edge lengths of the area L_1 and L_2, assume a hypothetical test line l_t parallel to L_2 and moving along the direction of L_1, as shown in Fig. C1. The test line is infinite long and its effective length in the area is L_2. According to geometric probability analysis (Underwood, 1970) for an arbitrarily-selected CNT, the probability to intersect with the test line is

$$p_{t-1} = \frac{\frac{1}{\pi/2}\int_0^{\pi/2} l_{CNT}\cos\theta \, d\theta}{L_1} = \frac{2}{\pi}\frac{l_{CNT}}{L_1}. \tag{C.1}$$

Picking a segment with the length of l_{CNT} from the test line randomly, the probability of two arbitrary CNTs intersect with each other is obtained as

$$p_{1-2} = p_{t-1}\frac{l_{CNT}}{L_2} = \frac{2}{\pi}\frac{l_{CNT}}{L_1}\frac{l_{CNT}}{L_2} = \frac{2}{\pi}\frac{l_{CNT}^2}{L_1 L_2}. \tag{C.2}$$

Considering the total number of CNTs in the area is N_{CNT}, the average intersection number of each CNT is

$$\bar{N}_{int} = p_{1-2}(N_{CNT} - 1) = \frac{2}{\pi}\frac{l_{CNT}^2}{L_1 L_2}(N_{CNT} - 1). \tag{C.3}$$

When the total number of CNTs in the area is large enough, i.e. $N_{CNT} \gg 1$, the average intersection number of each CNT is
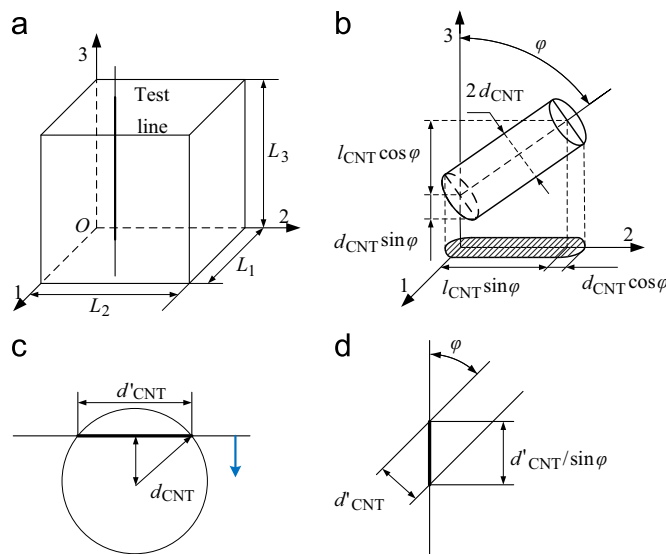

Fig. C2. Schematic diagram of the test-line method for the probability of two arbitrary CNTs intersecting with each other in 3D space: (a) the test line with effective length L_3 parallel to direction 3; (b) the projection of an arbitrary cylinder in plane 1-O-2; (c) the chord line in cross section of the cylinder; (d) the distance which the test line passes through when crossing the cylinder.

$$\bar{N}_{\text{int}} \approx \frac{2}{\pi} \frac{l_{\text{CNT}}^2}{L_1 L_2} N_{\text{CNT}} = \frac{2}{\pi} l_{\text{CNT}}^2 n_{\text{CNT}},$$

(C.4)

where $n_{\text{CNT}} = N_{\text{CNT}}/(L_1 L_2)$ is the average number of CNTs in a unit area.

C.2 Average intersection number of 3D networks

When λ_{CNT} is large enough, the probability of intersection between two CNTs with length of l_{CNT} and diameter of d_{CNT} is equivalent to that between a line segment with length of l_{CNT} and a cylinder with length of l_{CNT} and diameter of $2d_{\text{CNT}}$. As shown in Fig. C2(a), in a given cuboid of $L_1 \times L_2 \times L_3$, the test line is parallel to direction 3, and its effective length in the cuboid is L_3. The projection area of an arbitrary cylinder to the plane 1-O-2 is $2d_{\text{CNT}}(l_{\text{CNT}} \sin \varphi + \pi d_{\text{CNT}} \cos \varphi)$, as shown in Fig. C2(b). Then the probability for test line intersecting with cylinder is

$$p_{t-1}(\varphi) = \frac{2d_{\text{CNT}}(l_{\text{CNT}} \sin \varphi + \pi d_{\text{CNT}} \cos \varphi)}{L_1 L_2} \approx \frac{2l_{\text{CNT}} d_{\text{CNT}} \sin \varphi}{L_1 L_2}.$$

(C.5)

Picking a segment with the length of l_{CNT} from the test line randomly, the intersecting probability of the line segment and the cylinder is obtained as

$$p_{t-2}(\varphi) = \frac{l_{\text{CNT}} + s(\varphi)}{L_3},$$

(C.6)

where $s(\varphi)$ is the distance which test line passes through when crossing cylinder, and can be denoted as $s(\varphi) = d'_{\text{CNT}}/\sin \varphi$, as shown in Fig. C2(d). d'_{CNT} is the average chord length of the section area shown in Fig. C2(c), expressed as

$$d'_{\text{CNT}} = \frac{2}{d_{\text{CNT}}} \int_0^{d_{\text{CNT}}} \sqrt{d_{\text{CNT}}^2 - x^2} \, dx = \frac{\pi}{2} d_{\text{CNT}}.$$

(C.7)

Thus the probability of two CNTs intersecting with each other is obtained as

$$p_{1-2} = \int_0^{\pi/2} p_{t-1}(\varphi) p_{t-2}(\varphi) \sin \varphi \, d\varphi = \frac{\frac{\pi}{2} l_{\text{CNT}}^2 d_{\text{CNT}} + \pi l_{\text{CNT}} d_{\text{CNT}}^2}{L_1 L_2 L_3}$$

$$\approx \frac{\pi}{2} \frac{l_{\text{CNT}}^2 d_{\text{CNT}}}{L_1 L_2 L_3}.$$

(C.8)

For $N_{\text{CNT}} >> 1$, the average intersection number of each CNT is

$$\bar{N}_{\text{int}}^{\text{3D}} = p_{1-2}(N_{\text{CNT}} - 1) \approx \frac{\pi}{2} l_{\text{CNT}}^2 d_{\text{CNT}} n_{\text{CNT}}^{\text{3D}}.$$

(C.9)

C.3 Distribution of intersection number on CNTs

In both 2D and 3D models, for a network with N_{CNT} CNTs, intersection number of a CNT follows binomial probability distribution, and the probability that a CNT has k intersections is

$$P\{N_{\text{int}} = k\} = C_{N_{\text{CNT}}-1}^k p_{1-2}^k (1 - p_{1-2})^{N_{\text{CNT}}-1-k}, \quad k = 0, 1, \ldots, N_{\text{CNT}} - 1.$$

(C.10)

Here $C_{N_{\text{CNT}}-1}^k = \frac{[(N_{\text{CNT}} - 1)!]}{[k!(N_{\text{CNT}} - 1 - k)!]}$ is the binomial coefficient. If $(N_{\text{CNT}} - 1)$ is large, p_{1-2} small, and the expectation $\bar{N}_{\text{int}} = (N_{\text{CNT}} - 1)p_{1-2}$ appropriate, the probability distribution degrades to Poisson distribution as

$$P\{N_{\text{int}} = k\} = \frac{\bar{N}_{\text{int}}^k e^{-\bar{N}_{\text{int}}}}{k!}, \quad k = 0, 1, 2, \ldots, N_{\text{CNT}} - 1.$$

(C.11)

This result is consistent with the result of probability theory (Mendenhall et al., 2012) for big samples, which yields that the fraction of CNTs with k intersections is

$$\frac{N\{N_{\text{int}} = k\}}{N_{\text{CNT}}} = \frac{\bar{N}_{\text{int}}^k e^{-\bar{N}_{\text{int}}}}{k!}, \quad k = 0, 1, 2, \ldots, N_{\text{CNT}} - 1,$$

(C.12)

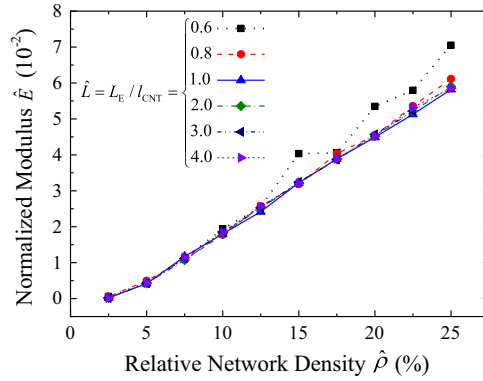where $N\{N_{\text{int}} = k\}$ is the number of CNTs with k intersections.

Fig. D1. Effect of area size on the normalized tensile modulus of 2D CNT networks.

Appendix D. FEM simulation on stiffness of 2D CNT networks

D.1 Numerical implementation in FEM

According to the periodic unit cell in Fig. 3(b), the FEM model is built, as shown in Fig. 3(c). The randomly distributed CNT networks are generated by a pre-process code, and their mechanical behaviors are simulated in the commercial FEM software ABAQUS/Standard (2005). The size of the periodic unit cell is $L_1 = L_2 = L_E$, and the thickness of the cell is taken as the diameter of the CNT.

In order to capture the essence of the network structure and speed up the simulation, the discrete CNTs with nonlinear constitutive behavior are simplified to elastic isotropic beams based on the continuum beam model (Berhan et al., 2004b; Papanikos et al., 2008; Wang and Wang, 2004; Wang et al., 2005), and planar quadratic beam elements (B22 of Abaqus/Standard, 2005) are used in the simulation. Besides, as discussed in Section 2.2.1, the interaction between two crossing CNTs at their intersection is simplified as a hinge. The periodic boundary conditions are applied on the unit cell by constraining nodes on opposite edges of the boundary (Chen and Ghosh, 2012; Segurado and Llorca, 2002; Wu and Koishi, 2009) as

$$u_\alpha^p - u_\alpha^{p'} = \varepsilon_{\alpha\beta}\left(x_\beta^p - x_\beta^{p'}\right) \quad (\alpha, \beta = 1, 2), \tag{D.1}$$

where p and p' are corresponding nodes of opposite edges of the unit cell, $\boldsymbol{\varepsilon}$ is strain tensor, $\boldsymbol{u}^p$ and $\boldsymbol{u}^{p'}$ are displacement of nodes p and p' respectively, and $\boldsymbol{x}^p$ and $\boldsymbol{x}^{p'}$ are the coordinates of nodes p and p' respectively. Besides, the rotation continuity of the boundary nodes on all the cut-and-moved CNTs is also taken into account as

$$\Delta\theta^p = \Delta\theta^{p'}. \tag{D.2}$$

D.2 Size effect and convergence study of 2D FEM model

The area convergence study is carried out before the stiffness analysis. For the CNTs with the aspect ratio $\lambda_{CNT} = l_{CNT}/d_{CNT} = 1000$, the periodic unit cells with different relative size, $\hat{L} = L_E/l_{CNT} = 0.6, 0.8, 1, 2, 3, 4$ are simulated, and the results are illustrated in Fig. D1. It is shown that the curves are consistent with each other for $\hat{L} \geq 1$. Therefore, in the following studies, the size of the periodic unit cell satisfies the condition of $\hat{L} \geq 1$ to eliminate the influence of the area size.

References

ABAQUS, 2005. ABAQUS/standard User's Manual, Version 6.5. Hibbitt, Karlsson, & Sorensen, Inc.

Aliev, A.E., Oh, J., Kozlov, M.E., Kuznetsov, A.A., Fang, S., Fonseca, A.F., Ovalle, R., Lima, M.D., Haque, M.H., Gartstein, Y.N., 2009. Giant-stroke, superelastic carbon nanotube aerogel muscles. Science 323, 1575–1578.

Allaoui, A., Bai, S., Cheng, H.-M., Bai, J., 2002. Mechanical and electrical properties of a MWNT/epoxy composite. Compos. Sci. Technol. 62, 1993–1998.

Balberg, I., Anderson, C., Alexander, S., Wagner, N., 1984. Excluded volume and its relation to the onset of percolation. Phys. Rev. B 30, 3933.

Banhart, F., 2001. The formation of a connection between carbon nanotubes in an electron beam. Nano Lett. 1, 329–332.

Bauhofer, W., Kovacs, J.Z., 2009. A review and analysis of electrical percolation in carbon nanotube polymer composites. Compos. Sci. Technol. 69, 1486–1498.

Baxter, S.C., Robinson, C.T., 2011. Pseudo-percolation: critical volume fractions and mechanical percolation in polymer nanocomposites. Compos. Sci. Technol. 71, 1273–1279.

Berhan, L., Yi, Y., Sastry, A., 2004a. Effect of nanorope waviness on the effective moduli of nanotube sheets. J. Appl. Phys. 95, 5027–5034.

Berhan, L., Yi, Y., Sastry, A., Munoz, E., Selvidge, M., Baughman, R., 2004b. Mechanical properties of nanotube sheets: alterations in joint morphology and achievable moduli in manufacturable materials. J. Appl. Phys. 95, 4335–4345.

Brady-Estévez, A.S., Kang, S., Elimelech, M., 2008. A single-walled-carbon-nanotube filter for removal of viral and bacterial pathogens. Small 4, 481–484.

Bryning, M.B., Milkie, D.E., Islam, M.F., Hough, L.A., Kikkawa, J.M., Yodh, A.G., 2007. Carbon nanotube aerogels. Adv. Mater. 19, 661–664.
Cao, A., Dickrell, P.L., Sawyer, W.G., Ghasemi-Nejhad, M.N., Ajayan, P.M., 2005. Super-compressible foamlike carbon nanotube films. Science 310, 1307–1310.
Celzard, A., Mareche, J., Furdin, G., 2005. Modelling of exfoliated graphite. Prog. Mater. Sci. 50, 93–179.
Chen, C., Lu, T., Fleck, N., 1999. Effect of imperfections on the yielding of two-dimensional foams. J. Mech. Phys. Solids 47, 2235–2272.
Chen, Y., Ghosh, S., 2012. Micromechanical analysis of strain rate-dependent deformation and failure in composite microstructures under dynamic loading conditions. Int. J. Plasticity 32, 218–247.
Chen, Y., Liu, B., He, X., Huang, Y., Hwang, K., 2010. Failure analysis and the optimal toughness design of carbon nanotube-reinforced composites. Compos. Sci. Technol. 70, 1360–1367.
Chen, Y., Liu, B., Hwang, K., Huang, Y., 2011. A theoretical evaluation of load transfer in multi-walled carbon nanotubes. Carbon 49, 193–197.
Chen, Y., Pan, F., Wang, S., Liu, B., Zhang, J., 2015a. Theoretical estimation on the percolation threshold for polymer matrix composites with hybrid fillers. Compos. Struct. 124, 292–299.
Chen, Y., Wang, S., Liu, B., Zhang, J., 2015b. Effects of geometrical and mechanical properties of fiber and matrix on composite fracture toughness. Compos. Struct. 122, 496–506.
Chiu, P., Duesberg, G., Dettlaff-Weglikowska, U., Roth, S., 2002. Interconnection of carbon nanotubes by chemical functionalization. Appl. Phys. Lett. 80, 3811–3813.
Christensen, R., 1986. Mechanics of low density materials. J. Mech. Phys. Solids 34, 563–578.
Christensen, R., Waals, F., 1972. Effective stiffness of randomly oriented fibre composites. J. Compos. Mater. 6, 518–535.
Cooper, S.M., Chuang, H.F., Cinke, M., Cruden, B.A., Meyyappan, M., 2003. Gas permeability of a buckypaper membrane. Nano Lett. 3, 189–192.
Cox, H., 1952. The elasticity and strength of paper and other fibrous materials. Br. J. Appl. Phys. 3, 72.
Deshpande, V., Ashby, M., Fleck, N., 2001. Foam topology: bending versus stretching dominated architectures. Acta Mater. 49, 1035–1040.
Ellenbroek, W.G., Mao, X., 2011. Rigidity percolation on the square lattice. Europhys. Lett. 96, 54002.
Foroughi, J., Spinks, G.M., Wallace, G.G., Oh, J., Kozlov, M.E., Fang, S., Mirfakhrai, T., Madden, J.D., Shin, M.K., Kim, S.J., 2011. Torsional carbon nanotube artificial muscles. Science 334, 494–497.
Gagné, M., Therriault, D., 2014. Lightning strike protection of composites. Prog. Aerosp. Sci. 64, 1–16.
Gibson, L.J., Ashby, M.F., 1999. Cellular solids: structure and properties, 2nd ed. Cambridge university press, Cambridge.
Gojny, F.H., Wichmann, M.H., Fiedler, B., Kinloch, I.A., Bauhofer, W., Windle, A.H., Schulte, K., 2006. Evaluation and identification of electrical and thermal conduction mechanisms in carbon nanotube/epoxy composites. Polymer 47, 2036–2045.
Gou, J., Tang, Y., Liang, F., Zhao, Z., Firsich, D., Fielding, J., 2010. Carbon nanofiber paper for lightning strike protection of composite materials. Composites Part B: Engineering 41, 192–198.
Grenestedt, J.L., 1998. Influence of wavy imperfections in cell walls on elastic stiffness of cellular solids. J. Mech. Phys. Solids 46, 29–50.
Gui, X., Wei, J., Wang, K., Cao, A., Zhu, H., Jia, Y., Shu, Q., Wu, D., 2010. Carbon nanotube sponges. Adv. Mater. 22, 617–621.
Halonen, N., Rautio, A., Leino, A.-R., Kyllonen, T., Toth, G., Lappalainen, J., Kordás, K., Huuhtanen, M., Keiski, R.L., Sápi, A., 2010. Three-dimensional carbon nanotube scaffolds as particulate filters and catalyst support membranes. ACS Nano 4, 2003–2008.
Head, D.A., Levine, A.J., MacKintosh, F.C., 2003. Deformation of cross-linked semiflexible polymer networks. Phys. Rev. Lett. 91, 108102.
Jacobs, D., Thorpe, M., 1996. Generic rigidity percolation in two dimensions. Phys. Rev. E 53, 3682.
Jin, M., Chen, C., Lu, T., 2013. The mechanical behavior of porous metal fiber sintered sheets. J. Mech. Phys. Solids 61, 161–174.
Jin, M., Zhao, T., Chen, C., 2014. The effects of micro-defects and crack on the mechanical properties of metal fiber sintered sheets. Int. J. Solids Struct. 51, 1946–1953.
Kellomäki, M., Åström, J., Timonen, J., 1996. Rigidity and dynamics of random spring networks. Phys. Rev. Lett. 77, 2730.
Kim, K.H., Vural, M., Islam, M.F., 2011. Single-walled carbon nanotube aerogel-based elastic conductors. Adv. Mater. 23, 2865–2869.
Koerner, H., Liu, W., Alexander, M., Mirau, P., Dowty, H., Vaia, R.A., 2005. Deformation–morphology correlations in electrically conductive carbon nanotube—thermoplastic polyurethane nanocomposites. Polymer 46, 4405–4420.
Kovacs, J.Z., Velagala, B.S., Schulte, K., Bauhofer, W., 2007. Two percolation thresholds in carbon nanotube epoxy composites. Compos. Sci. Technol. 67, 922–928.
Li, C., Thostenson, E.T., Chou, T.-W., 2008. Effect of nanotube waviness on the electrical conductivity of carbon nanotube-based composites. Compos. Sci. Technol. 68, 1445–1452.
Li, P., Zong, Y., Zhang, Y., Yang, M., Zhang, R., Li, S., Wei, F., 2013. In situ fabrication of depth-type hierarchical CNT/quartz fiber filters for high efficiency filtration of sub-micron aerosols and high water repellency. Nanoscale 5, 3367–3372.
Lu, L., Chen, W., 2010. Large-scale aligned carbon nanotubes from their purified, highly concentrated suspension. ACS Nano 4, 1042–1048.
Lu, W., Chou, T.-W., Thostenson, E.T., 2010. A three-dimensional model of electrical percolation thresholds in carbon nanotube-based composites. Appl. Phys. Lett. 96, 223106.
Lu, W., Zu, M., Byun, J.H., Kim, B.S., Chou, T.W., 2012. State of the art of carbon nanotube fibers: opportunities and challenges. Adv. Mater. 24, 1805–1833.
Ma, H., Gao, X.-L., 2008. A three-dimensional Monte Carlo model for electrically conductive polymer matrix composites filled with curved fibers. Polymer 49, 4230–4238.
Ma, W., Liu, L., Zhang, Z., Yang, R., Liu, G., Zhang, T., An, X., Yi, X., Ren, Y., Niu, Z., 2009. High-strength composite fibers: realizing true potential of carbon nanotubes in polymer matrix through continuous reticulate architecture and molecular level couplings. Nano Lett. 9, 2855–2861.
Matsumoto, M., Saito, S., Ohmine, I., 2002. Molecular dynamics simulation of the ice nucleation and growth process leading to water freezing. Nature 416, 409–413.
Mendenhall, W., Beaver, R., Beaver, B., 2012. Introduction to Probability and Statistics. Cengage Learning, USA.
Moisala, A., Li, Q., Kinloch, I., Windle, A., 2006. Thermal and electrical conductivity of single-and multi-walled carbon nanotube-epoxy composites. Compos. Sci. Technol 66, 1285–1288.
Moniruzzaman, M., Winey, K.I., 2006. Polymer nanocomposites containing carbon nanotubes. Macromolecules 39, 5194–5205.
Neda, Z., Florian, R., Brechet, Y., 1999. Reconsideration of continuum percolation of isotropically oriented sticks in three dimensions. Phys. Rev. E 59, 3717.
O'Brien, N., McCarthy, M., Curtin, W., 2013a. Improved inter-tube coupling in CNT bundles through carbon ion irradiation. Carbon 51, 173–184.
O'Brien, N., McCarthy, M., Curtin, W., 2013b. A theoretical quantification of the possible improvement in the mechanical properties of carbon nanotube bundles by carbon ion irradiation. Carbon 53, 346–356.
Oh, J.Y., Yang, S.J., Park, J.Y., Kim, T., Lee, K., Kim, Y.S., Han, H.N., Park, C.R., 2015. Easy preparation of self-assembled high-density buckypaper with enhanced mechanical properties. Nano Lett. 15, 190–197.
Papanikos, P., Nikolopoulos, D., Tserpes, K., 2008. Equivalent beams for carbon nanotubes. Comp. Mater. Sci. 43, 345–352.
Piper, N., Fu, Y., Tao, J., Yang, X., To, A., 2011. Vibration promotes heat welding of single-walled carbon nanotubes. Chem. Phys. Lett. 502, 231–234.
Sayago, I., Santos, H., Horrillo, M., Aleixandre, M., Fernandez, M., Terrado, E., Tacchini, I., Aroz, R., Maser, W., Benito, A., 2008. Carbon nanotube networks as gas sensors for NO_2 detection. Talanta 77, 758–764.
Segurado, J., Llorca, J., 2002. A numerical approximation to the elastic properties of sphere-reinforced composites. J. Mech. Phys. Solids 50, 2107–2121.
Slobodian, P., Riha, P., Lengálová, A., Svoboda, P., Sáha, P., 2011. Multi-wall carbon nanotube networks as potential resistive gas sensors for organic vapor detection. Carbon 49, 2499–2507.
Smajda, R., Kukovecz, Á., Kónya, Z., Kiricsi, I., 2007. Structure and gas permeability of multi-wall carbon nanotube buckypapers. Carbon 45, 1176–1184.
Stormer, B., Piper, N., Yang, X., Tao, J., Fu, Y., Kirca, M., To, A., 2012. Mechanical properties of SWNT X-Junctions through molecular dynamics simulation. Int. J. Smart Nano Mater. 3, 33–46.
Tang, L.-C., Zhang, H., Wu, X.-P., Zhang, Z., 2011a. A novel failure analysis of multi-walled carbon nanotubes in epoxy matrix. Polymer 52, 2070–2074.

Tang, L.C., Zhang, H., Han, J.H., Wu, X.P., Zhang, Z., 2011b. Fracture mechanisms of epoxy filled with ozone functionalized multi-wall carbon nanotubes. Compos. Sci. Technol. 72, 7–13.

Timoshenko, S.P., Young, D.H., 1945. Theory of Structures, 1st ed. McGraw-Hill, New York.

Underwood, E.E., 1970. Quantitative Stereology. Addison-Wesley Pub. Co..

Viswanathan, G., Kane, D.B., Lipowicz, P.J., 2004. High efficiency fine particulate filtration using carbon nanotube coatings. Adv. Mater. 16, 2045–2049.

Vohrer, U., Kolaric, I., Haque, M., Roth, S., Detlaff-Weglikowska, U., 2004. Carbon nanotube sheets for the use as artificial muscles. Carbon 42, 1159–1164.

Wang, B., Ma, Y., Li, N., Wu, Y., Li, F., Chen, Y., 2010. Facile and scalable fabrication of well-aligned and closely packed single-walled carbon nanotube films on various substrates. Adv. Mater. 22, 3067–3070.

Wang, C., Xie, B., Liu, Y., Xu, Z., 2012. Mechanotunable microstructures of carbon nanotube networks. ACS Macro Lett. 1, 1176–1179.

Wang, X., Wang, X., 2004. Numerical simulation for bending modulus of carbon nanotubes and some explanations for experiment. Composites Part B: Engineering 35, 79–86.

Wang, X., Wang, X., Xiao, J., 2005. A non-linear analysis of the bending modulus of carbon nanotubes with rippling deformations. Compos. Struct. 69, 315–321.

Wu, C., Koishi, M., 2009. A meshfree procedure for the microscopic analysis of particle-reinforced rubber compounds. Interact. Multiscale Mech. 2, 147–169.

Wu, Z., Chen, Z., Du, X., Logan, J.M., Sippel, J., Nikolou, M., Kamaras, K., Reynolds, J.R., Tanner, D.B., Hebard, A.F., 2004. Transparent, conductive carbon nanotube films. Science 305, 1273–1276.

Xie, B., Liu, Y., Ding, Y., Zheng, Q., Xu, Z., 2011. Mechanics of carbon nanotube networks: microstructural evolution and optimal design. Soft Matter 7, 10039–10047.

Xu, M., Futaba, D.N., Yamada, T., Yumura, M., Hata, K., 2010. Carbon nanotubes with temperature-invariant viscoelasticity from–196 to 1000 C. Science 330, 1364–1368.

Yang, Y., Gupta, M.C., Dudley, K.L., Lawrence, R.W., 2005. A comparative study of EMI shielding properties of carbon nanofiber and multi-walled carbon nanotube filled polymer composites. J. Nanosci. Nanotechnol. 5, 927–931.

Yi, Y., Berhan, L., Sastry, A., 2004. Statistical geometry of random fibrous networks, revisited: waviness, dimensionality, and percolation. J. Appl. Phys. 96, 1318–1327.

Zhang, M., Fang, S., Zakhidov, A.A., Lee, S.B., Aliev, A.E., Williams, C.D., Atkinson, K.R., Baughman, R.H., 2005. Strong, transparent, multifunctional, carbon nanotube sheets. Science 309, 1215–1219.

Zhang, Z., Liu, B., Zhang, Y.-W., Hwang, K.-C., Gao, H., 2014. Ultra-strong collagen-mimic carbon nanotube bundles. Carbon 77, 1040–1053.

Zhu, W., Ku, D., Zheng, J., Liang, Z., Wang, B., Zhang, C., Walsh, S., Au, G., Plichta, E., 2010. Buckypaper-based catalytic electrodes for improving platinum utilization and PEMFC's performance. Electrochim. Acta 55, 2555–2560.